

REPORT DOCUMENTATION PAGE

Form Approved
OMB No. 0704-0188

The public reporting burden for this collection of information is estimated to average 1 hour per response, including the time for reviewing instructions, searching existing data sources, gathering and maintaining the data needed, and completing and reviewing the collection of information. Send comments regarding this burden estimate or any other aspect of this collection of information, including suggestions for reducing the burden, to the Department of Defense, Executive Services and Communications Directorate (0704-0188). Respondents should be aware that notwithstanding any other provision of law, no person shall be subject to any penalty for failing to comply with a collection of information if it does not display a currently valid OMB control number.

PLEASE DO NOT RETURN YOUR FORM TO THE ABOVE ORGANIZATION.

1. REPORT DATE (DD-MM-YYYY) 30-06-2007		2. REPORT TYPE Final Performance Report		3. DATES COVERED (From - To) Feb. 15, 2004 to Jun. 30, 2007	
4. TITLE AND SUBTITLE Fundamental Studies in Embedded Ultrasonic NDE: Lamb Waves Interaction between Piezoelectric Wafer Active Sensors and Host Structures				5a. CONTRACT NUMBER	
				5b. GRANT NUMBER FA9550-0-0000-04-1-0085	
				5c. PROGRAM ELEMENT NUMBER	
6. AUTHOR(S) Yuh Chao				5d. PROJECT NUMBER	
				5e. TASK NUMBER	
				5f. WORK UNIT NUMBER	
7. PERFORMING ORGANIZATION NAME(S) AND ADDRESS(ES) The University of South Carolina 300 South Main St., RM #A222 Columbia, SC 29208				8. PERFORMING ORGANIZATION REPORT NUMBER	
9. SPONSORING/MONITORING AGENCY NAME(S) AND ADDRESS(ES) Air Force Office of Scientific Research AFOSR 875 N. Randolph St., RM 3112 Arlington, VA 22203-1768 <i>Dr Victor Gurquwtr/NA</i>				10. SPONSOR/MONITOR'S ACRONYM(S)	
				11. SPONSOR/MONITOR'S REPORT NUMBER(S)	
12. DISTRIBUTION/AVAILABILITY STATEMENT Approved for public release, distribution unlimited					
13. SUPPLEMENTARY NOTES					
14. ABSTRACT The emerging field of embedded ultrasonic NDE has the potential of producing fundamental changes in structural health monitoring, damage detection, and nondestructive evaluation by using small inexpensive and unobtrusive PWAS transducers that are permanently attached to the structure and can be interrogated at will. Unlike conventional ultrasonic transducers, PWAS are low-power non-resonant devices with broadband capabilities. PWAS are about the only transducers that can be embedded in large numbers in the structure without an exorbitant cost and weight penalty. Though the PWAS capabilities have been validated experimentally, the modeling of the PWAS behavior is still being developed. Fundamental aspects of the Lamb-wave interaction between PWAS and host structure during structural health monitoring need to be studied and understood.					
15. SUBJECT TERMS Embedded NDE, Fundamental Study, Piezoelectric, Piezoelectric Wafer Active Sensor					
16. SECURITY CLASSIFICATION OF:			17. LIMITATION OF ABSTRACT None	18. NUMBER OF PAGES 47	19a. NAME OF RESPONSIBLE PERSON Yuh Chao
a. REPORT unclassified	b. ABSTRACT unclassified	c. THIS PAGE unclassified			19b. TELEPHONE NUMBER (Include area code) (803)777-5869

AFRL-SR-AR-TR-07-0379

20071003425

FINAL TECHNICAL REPORT

to the

US AIR FORCE OFFICE OF SCIENTIFIC RESEARCH (AFOSR)

describing accomplishments in the

**FUNDAMENTAL STUDIES IN EMBEDDED ULTRASONIC NDE: LAMB WAVES INTERACTION
BETWEEN PIEZOELECTRIC WAFER ACTIVE SENSORS AND HOST STRUCTURE**

during the period of

February 15, 2004 to June 30, 2007

supported by

Grant No: FA9550-~~04-1-0005~~ 04-1-0005

Laboratory for Active Materials and Smart Structures

Submitted by the Principal Investigators

Victor Giurgiutiu, Professor (Feb. 15, 2004 to May 30, 2006)

and

Yuh Chao, Professor (June 1, 2006 to June 30, 2007)

Mechanical Engineering Department

University of South Carolina

300 South Main St., Columbia, SC 29208

STATUS OF EFFORT

The needs addressed by the project: Although piezoelectric wafer active sensors (PWAS) have shown remarkable experimental success, their modeling is still incomplete. PWAS are strongly coupled with the host structure through adhesive. PWAS are non-resonant broadband devices that excite the elastic waves through a “pinching” action (in-plane strain coupling). Many crucial questions still stand unanswered: *How powerful can PWAS be relative to their small size? How strong are the signals that PWAS can produce? How much power can be recovered at a receiver PWAS for a given power applied to the transmitter PWAS? Can one selectively excite various Lamb-wave modes (mode tuning)? Are there optimal operation conditions? How can one design an optimal PWAS?*

The proposed research generated necessary **theoretical modeling tools to answer fundamental questions related to the use of PWAS in embedded ultrasonic NDE and structural health monitoring**. It created a **comprehensive modeling and analysis methodology**, which can **expedit the technological development and reduce the maintenance burden of Air Force structure systems, while increasing safety and availability**.

The research consisted of analytical modeling, numerical simulation, and experimental validation. The project is built on the preliminary results demonstrated by the principal investigator. The study adopted the general approach used in the modeling of conventional guided-wave ultrasonic NDE and surface acoustic waves devices. Controlled experiments have been used to verify the predictions and to provide feedback for further theoretical developments.

GOALS AND OBJECTIVES

The goal of the research is to study **fundamental aspects of embedded ultrasonic NDE**. The scope is to develop a good understanding of the piezoelectric wafer active sensors (PWAS) interaction with the host structure during Lamb-wave structural health monitoring (SHM). The project has developed a comprehensive modeling and analysis methodology to understand how PWAS transducers can be optimally used to generate and detect Lamb-waves in thin-wall structures.

The main objectives that have been pursued in this project are:

- (a) The Lamb-waves excitation and detection with broadband PWAS transducers with selective tuning of various Lamb modes
- (b) In-situ immittance of PWAS transducers

ACCOMPLISHMENTS

-CRITICAL ISSUES RESOLVED BY THIS RESEARCH

The research started with the study of the interface between the PWAS and the structure. The effect of adhesive properties on the shear-lag transfer between PWAS and structure was assessed. Then, the plane-strain straight-crested Lamb-wave response under PWAS excitation was determined using the space-domain Fourier transform. For circular-crested waves, the axisymmetric problem was addressed with the Bessel functions formulation and the space-domain Hankel transform. **Lamb mode tuning** was demonstrated theoretically and verified experimentally. Certain Lamb wave modes were “dialed up” through the judicious selection of PWAS geometry and excitation frequency. Correlation with structural geometry and defect size was also pursued.

Next, the **in-situ PWAS immittance** was studied. The electro-acoustic transfer functions of the transmitting and receiving PWAS transducers were determined from the coupled analysis of the mechanical stress and strain and the electrical voltage and current simultaneously acting on the PWAS attached to the host structure. The Lamb modes expansion was used to predict the high-frequency immittance spectrum and compared it with experimental results.

1. TASK 1 – LAMB WAVES EXCITATION WITH BROADBAND PWAS TRANSDUCERS

For the modeling of a Lamb wave in a plate, we can use a 2-D model in rectangular or cylindrical coordinates. In the first case, we consider straight crested wave while in the second case we have circular crested wave. For straight crested Lamb waves, the theoretical model is supposed to be z -invariant, where the y direction is across the plate thickness and the x direction is within the plane of the plate. Rayleigh-

Lamb wave equation is, in both cases, $\frac{\tan(\beta d)}{\tan(\alpha d)} = - \left[\frac{4\xi^2 \alpha \beta}{(\xi^2 - \beta^2)^2} \right]^{\pm 1}$ where d is the half thickness of the

plate; $\alpha^2 = \frac{\omega^2}{c_p^2} - \xi^2$; $\beta^2 = \frac{\omega^2}{c_s^2} - \xi^2$; $\xi^2 = \frac{\omega^2}{c^2}$; c_p is the pressure velocity; c_s is the shear velocity; c is the

unknown phase velocity, and ξ is the wavenumber in the x and r direction respectively. The plus in the equation is for the symmetric case and the minus for the antisymmetric case. The phase velocity changes with the frequency and the thickness of the material. For each material exist a threshold value, which, depends on the material of the plate and the plate thickness, below which only S0 and A0 modes exist. At low frequencies, the A0 mode can be approximated with the flexural wave theory; in this case, the wave is highly dispersive and the wave packet spreads out with increasing frequency. At the same frequencies, the S0 can be approximated with the axial wave theory. The S0 is non-dispersive and shape of the wave

packet is preserved with the change of the frequency.

1.1. COUPLING BETWEEN STRUCTURE AND PWAS

Consider Lamb waves generated in a plate through surface mounted PWAS transducers bonded to the plate and connected to an alternating voltage source. Due to the alternating voltage applied between the PWAS electrodes, the piezoelectric transducer material undergoes an oscillatory expansion and contraction. The transducer is bonded to the plate with an adhesive layer. The contractions and expansion of the PWAS is transmitted to the material through the bonding layer. Figure 1b shows the PWAS bonded to the plate. Assume the PWAS has elastic modulus E_a and thickness t_a , the structure has elastic modulus E and thickness t , and the bond layer has shear modulus G_b and thickness t_b . The bond layer acts as a shear layer in which the mechanical effects are transmitted through the shear effects. The interfacial shear stress in bonding layer is expressed through the expression: $\tau(x) = \frac{t_a}{a} \frac{\psi}{\alpha + \psi} E_a \varepsilon_{ISA} \left(\Gamma a \frac{\sinh \Gamma x}{\cosh \Gamma a} \right)$ where α

is a coefficient that depends on the stress, strain and displacement distributions across the plate thickness and it is equal to 4 for low-frequencies dynamic conditions; ψ is the ratio $\psi = \frac{Et}{E_a t_a}$; ε_{ISA} is the induced strain in the PWAS by the electric voltage; Γ is the shear lag parameter and is a function of t_b , G_b and other variables. For ideal bonding, the shear stress in the bonding layer is: $\tau(x) = a\tau_0 [\delta(x-a) - \delta(x+a)]$

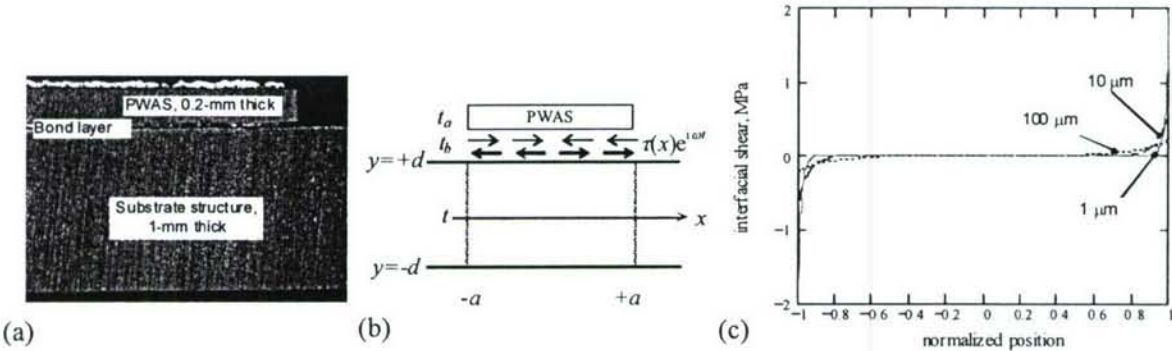


Figure 1 Shear layer interaction between PWAS and the host structure. (a) micrograph; (b) modeling; (c) variation of shear-lag transfer mechanism with bond thickness. APC-850 PWAS ($E_a=63$ GPa, $t_a=0.2$ mm, $l_a=7$ mm, $d_{31}=-175$ mm/kV) attached to a thin-wall aluminum structure ($E=70$ GPa, $t=1$ mm) through a bond layer of $G_b=2$ GPa

Figure 1c shows a characteristic plot of the interfacial shear stress along the length of the PWAS for different thickness of the bonded layers assuming $G_p = 2$ GPa. For thin layer of the bonded material ($1\mu\text{m}$), the shear stress is transmitted to the structure only at the ends of the PWAS. This is the ideal bonding solution, which can be considered true as a first approach to the problem.

1.2. SELECTIVE LAMB MODES EXCITATION WITH PWAS TRANSDUCERS

1.2.1. CLASSIC INTEGRAL TRANSFORM TECHNIQUE

PWAS transducers are capable of tuning into various guided wave modes. We developed a plane-strain analysis of the PWAS-structure interaction using the space-domain Fourier analysis; in this analysis the strain and displacement wave solutions for straight crested waves excited by a rectangular PWAS were studied. The basic assumption is the z -invariant motion supposing the PWAS is infinite in the z direction. The expression developed for strain is:

$$\varepsilon_x(x,t)|_{y=d} = -i \frac{\alpha \tau_0}{\mu} \left[\sum_{\xi^S} \sin(\xi^S a) \frac{N_S(\xi^S)}{D_S'(\xi^S)} e^{i(\xi^S x - \omega t)} + \sum_{\xi^A} \sin(\xi^A a) \frac{N_A(\xi^A)}{D_A'(\xi^A)} e^{i(\xi^A x - \omega t)} \right] \quad (1)$$

where $N_S = \xi\beta(\xi^2 + \beta^2)\cos(\alpha d)\cos(\beta d)$; $N_A = \xi\beta(\xi^2 + \beta^2)\sin(\alpha d)\sin(\beta d)$

$$D_S = (\xi^2 - \beta^2)^2 \cos(\alpha d)\sin(\beta d) + 4\xi^2\alpha\beta \sin(\alpha d)\cos(\beta d)$$

$$D_A = (\xi^2 - \beta^2)^2 \sin(\alpha d)\cos(\beta d) + 4\xi^2\alpha\beta \cos(\alpha d)\sin(\beta d)$$

ξ^S and ξ^A are the zeros of D_S and D_A respectively. We can note that these are the solutions of the Rayleigh-Lamb equation. The displacement wave solutions for circular crested waves excited by a round PWAS were studied by Raghavan and Cesnik (Raghavan and Cesnik 2004). The strain $\varepsilon_r(r,t)|_{z=d} = \partial u_r / \partial r$ derived from the displacement equation was:

$$\varepsilon_r(r,t)|_{z=d} = \pi \frac{\tau_0 a}{\mu} e^{j\omega t} \left[\sum_{\xi^S} J_1(\xi^S a) \xi^S \frac{N_S(\xi^S)}{D_S'(\xi^S)} H_1^{(2)}(\xi^S r) + \sum_{\xi^A} J_1(\xi^A a) \xi^A \frac{N_A(\xi^A)}{D_A'(\xi^A)} H_1^{(2)}(\xi^A r) \right] \quad (2)$$

where $H_1^{(2)}$ is the Henkel function of order 1 and second type.

1.2.2. NORMAL MODE EXPANSION TECHNIQUE

A different method, normal mode expansion (NME), can be used to determine the transducer frequencies for any kind of plates. In NME the fields generated in the structure due to the application of the surface loading are expanded in the form of an infinite series of the normal modes of the structure itself. It has been used for application as hollow cylinders excited by wedge transducers where the dispersion curves have a second order of infinity. For complete mathematical rigor of the NME method, it must be proofed that the field distribution of mode set is complete and orthogonal. We can assume that the set of acoustic waveguide mode functions is complete. We obtain that the acoustic field can be expressed as:

$$\mathbf{v}_i(y,z) = \sum_m a_m(z) \mathbf{v}_m(y) \quad (3)$$

$$\mathbf{T}_1(y, z) = \sum_m a_m(z) \mathbf{T}_m(y); \quad (4)$$

where

$$a_{\pm n}(z) = \frac{e^{\mp i\beta_n z}}{4P_{nn}} \bar{v}_{\pm n} \left(\frac{b}{2} \right) \cdot \int_{-\infty}^{\infty} e^{\pm i\beta_n \eta} \mathbf{t}(\eta) d\eta \quad (5)$$

$$P_{mm} = \text{Re} \frac{1}{2} \int_{-b/2}^{b/2} (-\bar{v}_m \cdot \mathbf{T}_m) \cdot \bar{z} dy \quad (6)$$

is the average power flow of the n^{th} mode in the z direction per unit waveguide width (in the x direction) and $\mathbf{t}(\eta)$ is the external traction exerted by the actuator..

1.2.3. IDEAL BONDING SOLUTION

In the case of ideal bonding solution, the shear stress in the bonding layer is concentrated at the ends.

$$\mathbf{t}(b/2, z) = \begin{cases} a\tau_0 [\delta(z-a) - \delta(z+a)] \mathbf{z} & \text{if } |z| \leq a \\ 0 & \text{if } |z| > a \end{cases} \quad (7)$$

Substituting (7) in (5), we obtain:

$$a_{\pm n}(z) = BE_{\pm n} e^{\mp i\beta_n z} F^{\pm} \quad (8)$$

Where

$$B = a\tau_0 \quad (9)$$

$$E_{\pm n} = \frac{\bar{v}_{\pm n z}(b/2)}{4P_{nn}} \quad (10)$$

$$F^{\pm} = \int_{-a}^a \delta(\eta-a) e^{\pm i\beta_n \eta} d\eta - \int_{-a}^a \delta(\eta+a) e^{\pm i\beta_n \eta} d\eta. \quad (11)$$

Function B is a constant depending on the excitation. Function E is the excitability function of mode v , and F is the excitation function. Solving the integral (11), we obtain:

$$F^{\pm} = \pm 2i \sin \beta_n a. \quad (12)$$

Substituting this equation in (8), we obtain:

$$a_{\pm n}(z) = ia\tau_0 \frac{\bar{v}_{nz}(b/2)}{2P_{nn}} \sin \beta_n a e^{\mp i\beta_n z} \quad (13)$$

The NME technique developed is valid for isotropic and non-isotropic materials. In the case of non-isotropic material the Poynting vector integral must be solved numerically. We will further expand equation (13) for the case of isotropic materials and we will compare the results with the classical integral transform solution and the experimental results.

(1) Symmetric Poynting Vector

For symmetric mode and isotropic material, displacements are:

$$u_{sz} = Bi\xi_S \cos(\alpha_S y) + C\beta_S \cos(\beta_S y)$$

$$u_{sy} = -B\alpha_S \sin(\alpha_S y) - Ci\xi_S \sin(\beta_S y)$$

where $B = 2i\xi_S \beta_S \cos(\beta_S d)$ and $C = (\xi_S^2 - \beta_S^2) \cos(\alpha_S d)$. For the range of interest of our experiments (0-1600 kHz mm), we can consider the ratio $c/c_s > 1$ always. Hence β is always real.

$$B \in \begin{cases} \text{Re if } \beta_S \in \text{Re} \\ \text{Im if } \beta_S \in \text{Im} \end{cases}, C \in \text{Re}$$

Case 1

$$\beta_S \in \text{Re} \left\{ \begin{array}{l} u_z \in \text{Complex} \\ u_y \in \text{Complex} \end{array} \right. \begin{cases} u_z = V_I + W_R \\ u_y = X_R + Y_I \\ v_z = -i\omega V_I - i\omega W_R \\ v_y = -i\omega X_R - i\omega Y_I \end{cases} \begin{cases} \bar{v}_z = -i\omega(V_I - W_R) \\ \bar{v}_y = i\omega(X_R - Y_I) \end{cases}$$

Case 2

$$\beta_S \in \text{Im} \left\{ \begin{array}{l} u_z \in \text{Complex} \\ u_y \in \text{Complex} \end{array} \right. \begin{cases} u_z = V_R + W_I \\ u_y = X_I + Y_R \\ v_z = -i\omega V_R - i\omega W_I \\ v_y = -i\omega X_I - i\omega Y_R \end{cases} \begin{cases} \bar{v}_z = i\omega(V_R - W_I) \\ \bar{v}_y = -i\omega(X_I - i\omega Y_R) \end{cases}$$

Case 2 is the same of case 1 but with the opposite sign:

$$\begin{cases} \bar{v}_z = \mp i\omega(V_I - W_R) \\ \bar{v}_y = \pm i\omega(X_R - Y_I) \end{cases}$$

where $V = Bi\xi_S \cos(\alpha_S y)$, $W = C\beta_S \cos(\beta_S y)$, $X = -B\alpha_S \sin(\alpha_S y)$, and $Y = -Ci\xi_S \sin(\beta_S y)$. The Poynting vector can be written as:

$$P_{mn} = \text{Re} \left[-\frac{1}{2} \int_{-b/2}^{b/2} (\bar{v}_y T_{yz} + \bar{v}_z T_{zx}) dy \right]$$

$$P_{mn} = \text{Re} \left[\mp \frac{i\omega}{2} \int_{-b/2}^{b/2} ((X_R - Y_I) T_{yz} - (V_I - W_R) T_{zx}) dy \right]$$

where

$$T_{yz} = \mu \left(\frac{\partial u_y}{\partial z} + \frac{\partial u_z}{\partial y} \right) \quad (14)$$

$$T_{zx} = (\lambda + 2\mu) \frac{\partial u_z}{\partial z} + \lambda \frac{\partial u_y}{\partial y} \quad (15)$$

Substituting the expression of the displacement, we obtain:

$$T_{yz} = \mu \begin{pmatrix} C(\xi_s^2 - \beta_s^2) \sin(\beta y) \\ -2iB\xi_s \alpha_s \sin(\alpha_s y) \end{pmatrix} e^{i(\xi_s z - \omega t)}$$

$$T_{zz} = \begin{bmatrix} -[\lambda \alpha_s^2 + \xi_s^2 (\lambda + 2\mu)] B \cos(\alpha_s y) \\ +i2\mu \xi_s \beta_s C \cos(\beta_s y) \end{bmatrix} e^{i(\xi_s z - \omega t)}$$

The expression in brackets of the first term of the left hand side can be rearranged as:

$$\begin{aligned} (\lambda + 2\mu) \xi_s^2 + \lambda \alpha_s^2 &= (\lambda + 2\mu) (\xi_s^2 + \alpha_s^2) - 2\mu \alpha_s^2 \\ &= -2\mu \alpha_s^2 + (\lambda + 2\mu) \xi_s^2 + (\lambda + 2\mu) \frac{\omega^2}{c_p^2} - (\lambda + 2\mu) \xi_s^2 \\ &= -2\mu \alpha_s^2 + (\lambda + 2\mu) \frac{\omega^2}{c_p^2} \end{aligned}$$

Equation (8) becomes:

$$a_{\pm n}(z) = \mp \frac{\alpha \tau_0}{\mu} \frac{\begin{bmatrix} Bi\xi_s \cos(\alpha_s d) \\ -C\beta_s \cos(\beta_s d) \end{bmatrix}}{P_{nn}} \sin(\beta_s a) e^{\mp i\beta_s z}$$

The strain can be derived as:

$$\begin{aligned} \varepsilon_z &= \frac{\partial u_z}{\partial z} = \frac{\partial \int v_z(z, y, t) dt}{\partial z} = \frac{\partial a(z) v(y) \int e^{-i\omega t} dt}{\partial z} \\ \varepsilon_z &= \frac{i}{\omega} \frac{\partial a(z)}{\partial z} v(y) e^{-i\omega t} = \pm \frac{\xi}{\omega} a(z) v(y) e^{-i\omega t} \end{aligned}$$

(2) Antisymmetric Poynting Vector

For antisymmetric mode and isotropic material, displacements are:

$$\begin{aligned} u_z^A(z, y, t) &= (i\xi_A A \sin \alpha_A y - \beta_A D \sin \beta_A y) e^{i(\xi_A z - \omega t)} \\ u_y^A(z, y, t) &= (\alpha_A A \cos \alpha_A y - i\xi_A D \cos \beta_A y) e^{i(\xi_A z - \omega t)} \end{aligned}$$

where $A = 2i\xi_A \beta_A \sin(\beta_A d)$ and $D = -(\xi_A^2 - \beta_A^2) \sin(\alpha_A d)$. α_A is real if $\frac{\omega^2}{c_p^2} - \xi^2 \geq 0$, hence

$$\frac{\omega^2}{c_p^2} - \frac{\omega^2}{c^2} \geq 0, \quad \frac{c^2 - c_s^2}{c^2 c_p^2} \geq 0 \quad \text{or} \quad \frac{c^2}{c_p^2} \geq 1, \quad \frac{c}{c_p} \geq 1.$$

$$\begin{aligned} (\lambda + 2\mu) \xi_s^2 + \lambda \alpha_s^2 &= \mu \frac{\omega^2}{c_s^2} - \mu \xi_s^2 + \mu \xi_s^2 - 2\mu \alpha_s^2 \\ &= -2\mu \alpha_s^2 + \mu \beta_s^2 + \mu \xi_s^2 = \mu (\xi_s^2 + \beta_s^2 - 2\alpha_s^2) \end{aligned} \tag{16}$$

Hence

$$T_{zz} = \mu \left[\begin{array}{l} -(\xi_s^2 + \beta_s^2 - 2\alpha_s^2) B \cos(\alpha_s y) \\ + 2i\xi_s \beta_s C \cos(\beta_s y) \end{array} \right] e^{i(\xi_s z - \omega t)}$$

Upon substitution in the Poynting vector and after solving the integral, we obtain:

$$P_{nm} = \mp \text{Re} \frac{\omega \mu}{2} \left[\begin{array}{l} -\xi_s (\xi_s^2 + \beta_s^2) (B^2 + C^2) d + C^2 \xi_s (\xi_s^2 - 3\beta_s^2) \frac{\sin \beta_s d \cos \beta_s d}{\beta_s} \\ -\xi_s (\xi_s^2 + \beta_s^2 - 4\alpha_s^2) B^2 \frac{\sin \alpha_s d \cos \alpha_s d}{\alpha_s} \\ i(\alpha_s + \beta_s) [\xi_s^2 + \alpha_s \beta_s + \beta_s (\alpha_s - \beta_s)] BC \frac{\sin(\alpha_s - \beta_s) d}{(\alpha_s - \beta_s)} \\ -i(\alpha_s - \beta_s) [\xi_s^2 - \alpha_s \beta_s - \beta_s (\alpha_s + \beta_s)] BC \frac{\sin(\alpha_s + \beta_s) d}{(\alpha_s + \beta_s)} \end{array} \right]$$

For the first mode of propagation the ratio c/c_p is always less than 1 because $c/c_p < c/c_s < 1$, hence α is always imaginary; β is always imaginary.

$$A \in \text{Im} \quad \forall \alpha_A, \beta_A, D \in \text{Im} \quad (\text{if } \alpha_A \in \text{Im})$$

For

$$\alpha_A \in \text{Im} \left\{ \begin{array}{l} u_z \in \text{Re} \left\{ \begin{array}{l} v_z = -i\omega u_z \in \text{Im} \\ \tilde{v}_z = i\omega u_z \end{array} \right. \\ u_y \in \text{Im} \left\{ \begin{array}{l} v_y = -i\omega u_y \in \text{Re} \\ \tilde{v}_y = -i\omega u_y \end{array} \right. \end{array} \right. \quad (17)$$

The Poynting vector can be written as:

$$P_{nm} = \text{Re} \left[-\frac{1}{2} \int_{-d}^d (\tilde{v}_y T_{yz} + \tilde{v}_z T_{zz}) dy \right] \quad (18)$$

Substituting (22) in (23) we have:

$$P_{nm} = \text{Re} \left[-\frac{1}{2} \int_{-d}^d (i\omega u_y T_{yz} - i\omega u_z T_{zz}) dy \right] \quad (19)$$

or

$$P_{nm} = \text{Re} \left[-\frac{i\omega}{2} \int_{-d}^d (u_y T_{yz} - u_z T_{zz}) dy \right]$$

For antisymmetric displacements, Equations (18) and (19) become:

$$T_{yzA} = \mu \left(\begin{array}{l} 2i\xi_A \alpha_A A \cos(\alpha_A y) \\ + (\xi_A^2 - \beta_A^2) D \cos(\beta_A y) \end{array} \right) e^{i(\xi_A z - \omega t)}$$

$$T_{zz} = - \left[\begin{array}{l} [(\lambda + 2\mu) \xi_A^2 + \lambda \alpha_A^2] A \sin(\alpha_A y) \\ + 2i\mu \xi_A \beta_A D \sin(\beta_A y) \end{array} \right] e^{i(\xi_A z - \omega t)}$$

Substituting (20) in the latter, we obtain:

$$T_{zz} = -\mu \left[\begin{array}{l} (\xi_A^2 + \beta_A^2 - 2\alpha_A^2) A \sin(\alpha_A y) \\ + 2i\xi_A \beta_A D \sin(\beta_A y) \end{array} \right] e^{i(\xi_A z - \omega t)}$$

The Poynting vector (24) becomes upon substitution and integration

$$P_{nn} = -\frac{\omega\mu}{2} \operatorname{Re} \left[i \left[\begin{array}{l} -i\xi_A D^2 (\xi_A^2 - 3\beta_A^2) \frac{\sin(\beta_A d) \cos(\beta_A d)}{\beta_A} + i\xi_A (A^2 - D^2) d (\xi_A^2 + \beta_A^2) \\ -i\xi_A A^2 (\xi_A^2 + \beta_A^2 - 4\alpha_A^2) \frac{\sin(\alpha_A d) \cos(\alpha_A d)}{\alpha_A} \\ + (\alpha_A - \beta_A) [3\xi_A^2 + \alpha_A \beta_A + \beta_A (\alpha_A + \beta_A)] AD \frac{\sin[(\alpha_A - \beta_A) d]}{(\alpha_A - \beta_A)} \\ + (\alpha_A + \beta_A) [3\xi_A^2 - \alpha_A \beta_A - \beta_A (\alpha_A - \beta_A)] AD \frac{\sin[(\alpha_A + \beta_A) d]}{(\alpha_A + \beta_A)} \end{array} \right] \right]$$

Equation (8) becomes:

$$a_{zn}(z) = \mp \frac{\alpha \tau_0}{\mu} \frac{u_z(d)}{P_{nn}} \sin(\beta_A a) e^{\mp i\beta_A z}$$

The strain can be derived as:

$$\begin{aligned} \varepsilon_z &= \frac{\partial u_z}{\partial z} = \frac{\partial \int v_z(z, y, t) dt}{\partial z} = \frac{\partial a(z) v(y) \int e^{-i\omega t} dt}{\partial z} \\ \varepsilon_z &= \frac{i}{\omega} \frac{\partial a(z)}{\partial z} v(y) e^{-i\omega t} = \pm \frac{\xi}{\omega} a(z) v(y) e^{-i\omega t} \\ \varepsilon_z &= -\frac{\alpha \tau_0}{\mu} \frac{\xi_A}{\omega} \frac{u_z(d)}{P_{nn}} \sin(\beta_A a) e^{\mp i\beta_A z} v(y) e^{-i\omega t} \end{aligned}$$

2. TASK 2 – IN-SITU IMMITTANCE OF PWAS TRANSDUCERS

The electro-acoustic transfer functions of the transmitting and receiving PWAS transducers are determined by the stress and strain coupling between the PWAS and the host structure. For a PWAS transducer, the input immittance will depend on the intrinsic transducer capacitance C and on the effects of acoustic radiation. In our investigation, we started from the simulation and experimental verification for the immittance of free PWAS and then moved to the structure constrained bonded PWAS. We also extended our analysis to numerical simulation of propagating Lamb waves excited through PWAS transducers in the structure.

2.1. NUMERICAL SIMULATION OF ELECTRO/MECHANICAL IMPEDANCE OF FREE PWAS

The E/M impedance technique utilizes the direct and the converse electro-mechanical properties of piezoelectric materials, allowing for the simultaneous actuation and sensing of the structural response. The variation of the electro-mechanical impedance of piezoelectric sensor-actuators (wafer transducers)

intimately bonded to the structure is monitored over a large frequency spectrum in the high kHz frequency band. Their frequency response, the measured impedance parameters such as real and imaginary parts, amplitude, phase, etc. serve as potential indicators of structural damage and reflects the state of structural integrity. We started the impedance simulation with square and circular free PWAS. Free PWAS were modeled with finite element coupled filed elements. Then time harmonic analyses were performed on the free PWAS to obtain the electrical charge. With the data of electrical charge we then calculated the electromechanical (E/M) impedance of the PWAS.

To employ the coupled field analysis of PWAS, coupled filed elements which could deal with both mechanical and electrical fields are used to model the PWAS. The coupled field finite element we used is a 3-D brick element that has eight nodes with up to six degrees of freedom at each node. When used for piezoelectric analysis, it could have an extra electrical voltage DOF in addition to these displacement DOFs; for each DOF of a node, there is a reaction force. Reaction force F_X, F_Y, F_Z corresponds to the X, Y, Z displacement DOFs respectively and charge Q corresponds to the voltage DOF. We utilized this charge Q to calculate the impedance data. For the coupled filed piezoelectric analysis, stress field and electric field are coupled together so that change in one field will induce change in the other field. Thus alternating electric voltage V can be direct applied on the coupled field elements as constrains and electrical charge will accumulate as reaction force Q , and impedance Z is calculated as V/I where I is the current value and V is the applied potential voltage. The current I comes from the accumulated charge on the electrode surface of PWAS and it calculated as $I = j\omega \sum Q_i$, where ω is the operating frequency, $j = \sqrt{-1}$ and $\sum Q_i$ is the summed nodal charge (nodal reaction load). When excited by an alternating electric voltage the free PWAS acts as an electromechanical resonator. The modeling of a free PWAS is useful for the understanding the electromechanical coupling between the mechanical vibration response and the complex electrical response of the sensor.

Harmonic analysis was performed on the square and circular PWAS model to obtain the frequency response of the electrical mechanical impedance. In the Harmonic analysis, excitation of sinusoidal voltage was applied on the nodes at the top and bottom surface. The excitation signal will sweep a certain frequency range as the commercial impedance analyzer does. When excited with alternating voltage, electrical charge, i.e. the reaction force Q to the electrical potential was accumulated on the nodes at the surface of PWAS elements. Then the impedance Z at sensor terminals is calculated as V/I where I is the current and V is the applied potential.

The meshed squared PWAS is shown in Figure 2. The square is 7mm long, 7 mm wide and 0.2 mm thick. The circular PWAS has a diameter of 7mm and a thickness of 0.2mm. The simulation of PWAS is simplified by the use of symmetry conditions. Only the top right quarter of the PAS was modeled to utilize the symmetry characteristic of the model. The PWAS was modeled using 3-D 8 nodes coupled

field element that has 4 degrees of freedom at each node. This brick coupled field element is capable of modeling piezoelectric materials with its **VOLTAGE** degree of freedom activated. For the nodes at both the top and bottom surface, their **VOLTAGE** DOF were coupled to only one master node to simulate the electrode surface of the PWAS. It will also simplify the solution process and thus can yields a faster solution. When a PWAS is excited either electrically or mechanically, resonance may happen when the response is very large. There could be of two types of resonance:

- Electromechanical resonances
- Mechanical resonances

Mechanical response takes place in the same condition as in a conventional elastic structure while electromechanical resonances are specific to piezoelectric materials. Electromechanical resonances reflect the coupling between the mechanical and electrical variables, they happen under electric excitation, which produces electromechanical responses (i.e., both a mechanical vibration and a change in the electric admittance and impedance). When a PWAS is excited

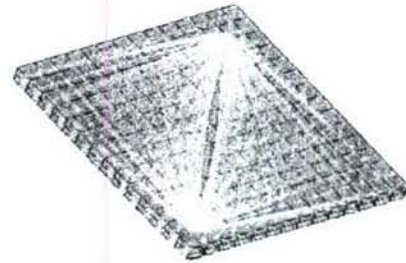


Figure 3 3-D mesh of square PWAS with boundary conditions

harmonically with a constant voltage at a given frequency, electrical resonance is associated with the situation in which a device is drawing very large currents. At resonance, the admittance becomes very large while the impedance goes to zero. As the admittance becomes very large, the current drawn under constant-voltage excitation also becomes very large because $I=Y \cdot U$. In piezoelectric devices, the mechanical response at electrical resonance also becomes very large. This happens because the electromechanical coupling of the piezoelectric materials transfers energy from the electrical input into the mechanical response.

Figure 4a and Figure 4b show the log-scale real and imaginary in which we can see the resonance part of frequency response of admittance for a square PWAS ($l=7$ m, $b=7$ mm, $h=0.2$ mm,APC 850 Piezoceramic) excited by electrical potential signal sweeping from 100KHz to 1MHz. These figures show some of the resonance behavior patterns of resonance, such as zigzags of the imaginary part and a sharp peak of the real part.

To verify the result of the frequency response of PWAS E/M impedance, the simulation result was compared to the experimental data acquired with the HP 4194A Impedance Analyzer. The impedance measurements were done with 7 mm square PWAS ($l=7$ mm, $b=7$ mm, $t=0.2$ mm, APC 850 Piezoceramic). The comparison was plotted in Figure 5a and Figure 5b. From these comparisons we can see that the experimental results are in fairly good agreement with the simulated result especially for the relative low frequency range. The experimental curve shows an additional peak at around 920 kHz and that may be due to the edge roughness generated during the manufacturing process.

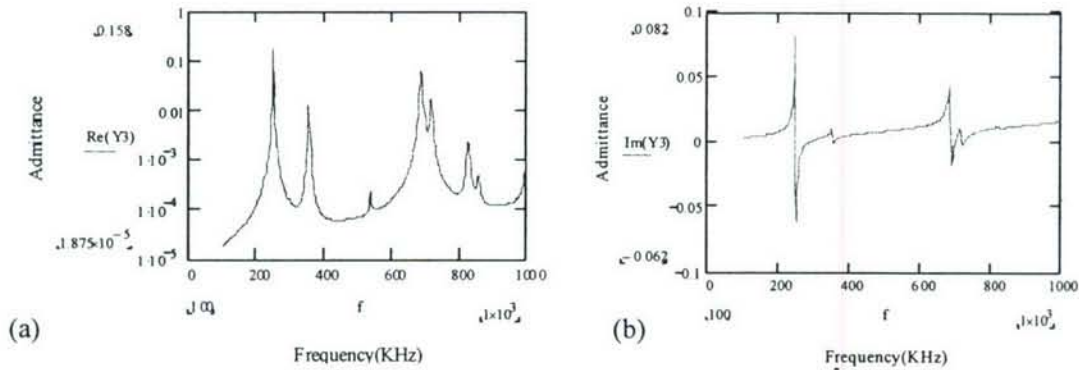


Figure 4 Frequency response of admittance of square PWAS (100 kHz – 1 MHz). (a) real part; (b) imaginary part

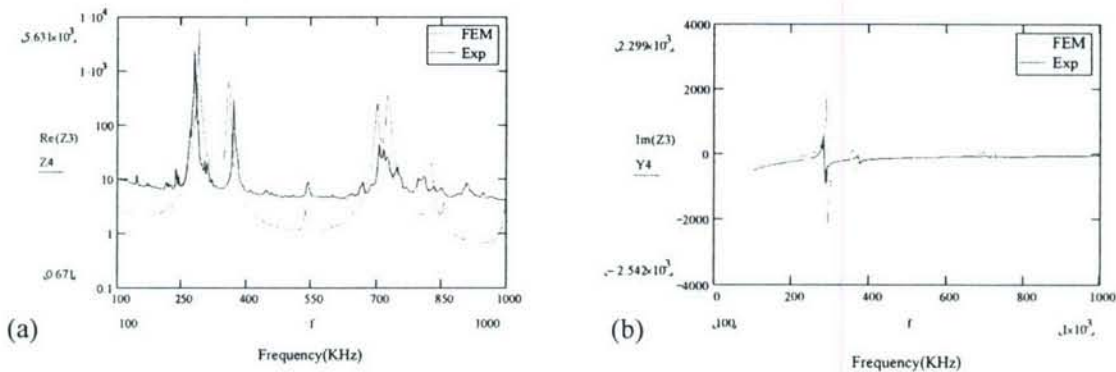


Figure 5 Comparison of frequency response of impedance of square PWAS between simulated data and experimental result (100 kHz – 2 MHz). (a) real part; (b) imaginary part

We continued our analysis on the circular PWAS with the same technique using an FE model of the circular PWAS that has a diameter of 7mm and a thickness of 0.2mm. Admittance plots of circular PWAS were given in Figure 6a and Figure 6b. Four resonance peaks were clearly visible and these peaks corresponded to the first four in-plane radical motion mode. The simulated impedance data was then compared to the impedance measurements of circular PWAS and the comparison were given in Figure 7a and Figure 7b. These comparisons indicated a good agreement between finite element simulation and experiments. We can also see that in high frequency range (1500 kHz – 2000 kHz), the simulated impedance peaks shifted a little from that of the experimental measurements, that may be explained that the element size and time step of harmonic analysis may not be appropriate at such high frequencies and thus can not yield the correct results. The effect of element size and time step at high frequencies will be explored in future work. According to previous discussion and comparisons, the overall conclusion could be made that good agreement between the FE simulation of E/M impedance of free PWAS and experimental data can be obtained with the coupled field analysis.

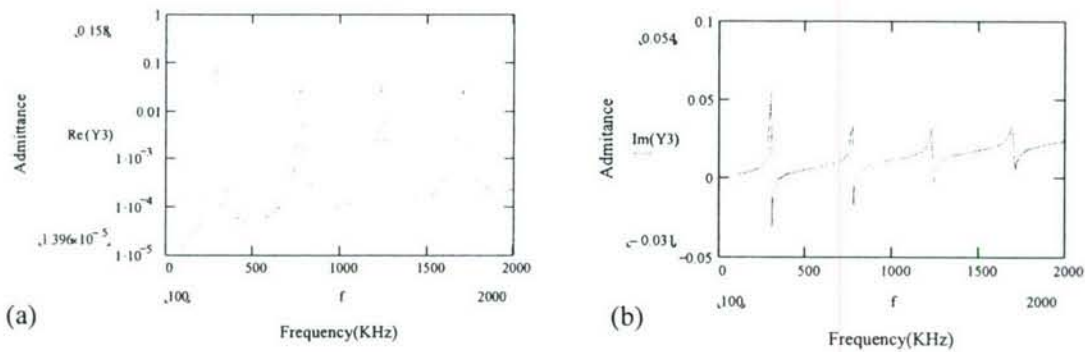


Figure 6 Frequency response of admittance of circular PWAS (100 kHz – 1 MHz). (a) real part; (b) imaginary part

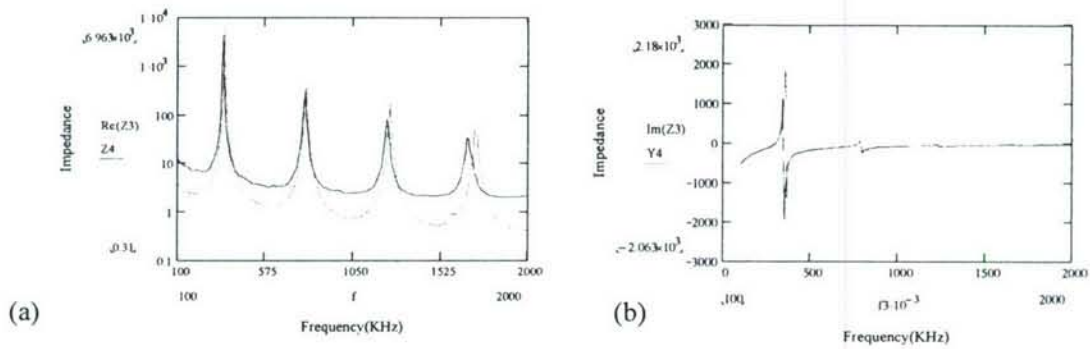


Figure 7 Comparison of frequency response of impedance of circular PWAS between simulated data and experimental result (100 kHz – 2 MHz). (a) real part; (b) imaginary part

2.2. NUMERICAL SIMULATION OF ELECTRO/MECHANICAL IMPEDANCE OF STRUCTURE CONSTRAINED PWAS

This section presents the E/M impedance analysis of structures constrained PWAS. As stated in previous section, the electro-mechanical (E/M) impedance method uses in-plane surface excitation to measure the point wise mechanical impedance of the structure through the real part of the electrical impedance measured at the sensor terminals. The measured impedance parameters such as real and imaginary parts, amplitude, phase, etc. serve as potential indicators of structural damage. In this section we will first examine the analytical solution of the structure constrained PWAS E/M impedance; second pure structure FE analysis will be performed to infer the structure stiffness and then the PWAS impedance with the analytical equations. Finally we will model the structure and the PWAS with coupled field element to achieve a direct simulation of PWAS E/M impedance.

2.2.1. ANALYTICAL IMPEDANCE ANALYSIS OF 1-D BEAM WITH PWAS

Consider a constrained PZT active sensor of length l_a , thickness t_a and width b_a that undergoes longitudinal expansion (u_1) induced by the thickness polarization electric field as shown in Figure 8. The electric field ($E = V/t_a$) is produced by the application of a harmonic voltage ($V(t) = Ve^{i\omega t}$) between the top and bottom surface (electrodes). When the PWAS is bonded to the structure, the structure will constrain the PWAS motion with a structural stiffness k_{str} . The overall structural stiffness, k_{str} , has been split into two end components, each of size $2k_{str}$ for symmetry. The admittance and impedance expressions for a PZT active sensor constrained by the structural substrate are

$$Y = i\omega \cdot C \left[1 - \kappa_{31}^2 \left(1 - \frac{1}{\varphi \cot \varphi + r} \right) \right] \quad (20)$$

$$Z = \frac{1}{i\omega \cdot C} \left[1 - \kappa_{31}^2 \left(1 - \frac{1}{\varphi \cot \varphi + r} \right) \right]^{-1} \quad (21)$$

In that equation equivalent stiffness ratio $r = \frac{k_{str}}{r_{PZT}}$, C and κ_{31}^2 are PWAS related constants and φ are notation related to wave length and PWAS dimension.

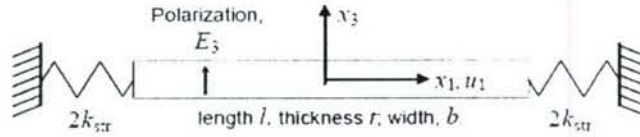


Figure 8 PZT wafer active sensor constrained by an overall structural stiffness, k_{str}

2.2.2. PWAS E/M IMPEDANCE ANALYSIS OF 1-D BEAM WITH FE STRUCTURE SIMULATION

One-dimensional beam structures are easy to model, and the prediction of their natural frequencies and vibration modes are fairly well understood, so a natural idea is to instrument the beam with PWAS and study the dynamic characteristic of the beam through the frequency response of impedance. One further step will be to perform damage detection of the beam structure when cracks are created on it. From the above analytical discussion, we can see if we can find the structure stiffness, with the above equation, E/M impedance can be obtained. The structure stiffness k_{str} of the beam can be derived by calculating the response of structural substrate using the general theory of structural vibrations, thus the analytical solution of the E/M impedance of 1-D beam constrained PWAS can be obtained. We can also employ FEM to get the structure stiffness and calculate the impedance consequently. So, we will perform FE

structure analysis on the structure to get the structure stiffness and then infer the E/M impedance. On the 1-D beam model, the PWAS is installed at the location of 40 mm from left hand end with standard sensor-installation procedure. The size of the PWAS is almost the same as the height of the beam, so the movement in longitude direction dominates, thus simplify the analysis. When the PWAS is excited, it will exert force and bending moment onto the beam. The piezoelectric wafer is also intimately bonded to the structure, such that the strain/displacement compatibility and stress/force equilibrium principles apply. As the PZT material is activated electrically, strain is induced in the piezoelectric wafer, and interaction forces and moments appear at the interface between the sensor and the structure. In the pin-force model, the interaction force, F_{PZT} , is assumed to act at the sensor boundary only. Induced by F_{PZT} are activation forces and moments (N_a and M_a), which apply a pinching action to the structural surface and generate structural waves.

$$F_{PZT} = |F_{PZT}| \cdot e^{i\omega t}, N_a = F_{PZT}, M_a = F_{PZT} \cdot \frac{h}{2} \quad (22)$$

The beam was modeled with shell element. Harmonic excitation of force and moment were exerted at the borders of the PWAS to simulate the presence of the PWAS. The frequency response of the structure was then obtained through harmonic analysis. Two DOFs, translation displacement in X direction UX and rotation displacement in Y ROTY are used to calculate the structure frequency response function (FRF) when harmonic analysis at the frequency range from 10 KHz to 300 KHz was performed. The relative movement between the two edge points was used to calculate the axial and flexural frequency responses function. Then overall structure stiffness was then obtained and substituted into the impedance and admittance equation. Finally the FE derived impedance is compared to the analytical results and experimental results acquired with commercial impedance analyzer as shown in Figure 9. We can see that these results are in good agreement.

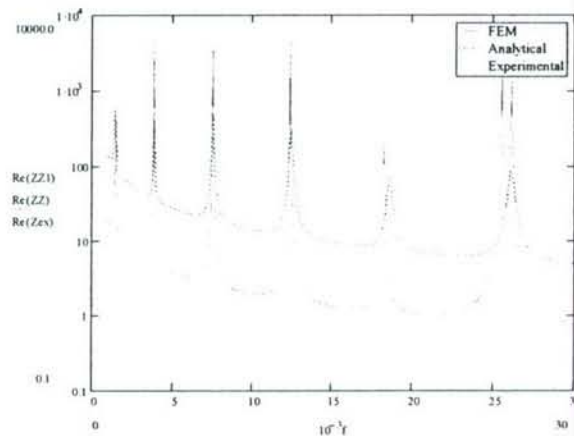


Figure 9 Comparison of the real part impedance of PWAS attached on the 1-D beam showed good agreement

2.2.3. IMPEDANCE ANALYSIS OF 1-D BEAM WITH PWAS USING COUPLED FIELD FINITE ELEMENT METHOD

The next step is to simulate the 1-D beam structure and PWAS with coupled field element. With brick coupled field element, the direct interaction between mechanical motion and electrical potentials could be modeled in a nature way. The narrow beam and square PWAS were modeled with 3-d elements and the PWAS was bonded on the surface of the beam structure. Different materials properties, steel and piezoelectric material APC 850 were specified on the two objects modeled with different elements. The adjacent nodes between the beam and the PWAS were “glued” together in ANSYS, which means the strain and stress can be transferred from one of them to the other. Voltage DOFs were coupled for the nodes of the PWAS at both the top and bottom surface to simulate the electrodes. Harmonic analysis was performed to acquire the impedance data of the PWAS as done in the free PWAS analysis. Finally, the comparison plot of impedance real part between experimental result, non coupled field FE simulation and coupled field FE simulation was presented in Figure 10. From the comparison we can see that the impedance data obtained from the coupled field analysis was very closely to the experimental structure impedance data. These results validate the possibility of using the coupled field method to analyze and simulate the structure with piezoelectric sensors.

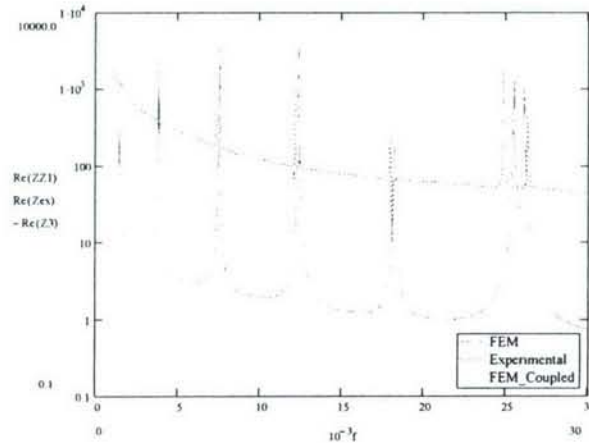


Figure 10 Comparison of the real part impedance of PWAS attached on the 1-D beam showed good agreement

2.3. NUMERICAL SIMULATION OF WAVE PROPAGATION WITH PWAS

2.3.1. WAVE PROPAGATION SIMULATION

In this section we study the wave propagation in structures excited by PWAS. Our investigation was first focused on simple 1-D wave-propagation studies that allow a simpler analysis and foster rapid understanding. A narrow-strip aluminum beam (914mm long, 8 mm wide and 1.6 mm thick) as shown in Figure 11a was modeled using four-node shell element that has six degrees of freedom at each node. The

shell element displayed both bending and membrane capabilities. The FEM also permitted the simulation of cracks through the thickness. Figure 11b shows a simulated crack placed transverse to the beam, along the transverse symmetry line. The crack length is dictated by the number of released nodes. In order to obtain better resolution for crack simulation, the discretization mesh was locally refined, as indicated in Figure 11b.

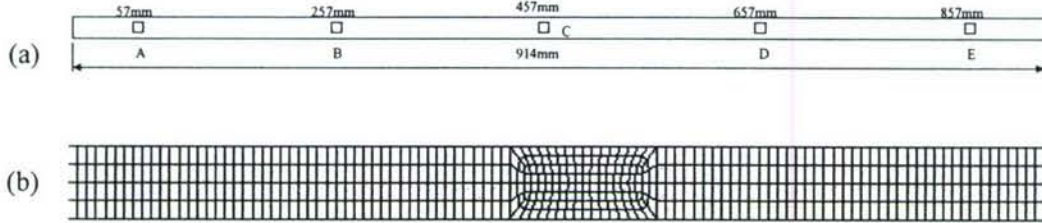


Figure 11 Wave propagation simulation (a) Narrow aluminum beam with PWAS sensors; (b) Mesh design of the beam and crack refinement (center part)

To model the wave excitation and reception process, we first define several groups of finite elements that cover certain areas on the beam to represent piezoelectric active sensor. The locations of these sensor areas were shown in Figure 11a. We can then apply excitations on these equivalent sensor areas and examine the mechanical response acquired at simulated sensor areas. The positions of these sensors were shown in Figure 11a. The excitation signal considered in our studies consisted of a smoothed tone burst. The smoothed tone burst was obtained from a pure tone burst of frequency f filtered through a Hanning window. The Hanning window was described by the equation:

$$x(t) = \frac{1}{2} [1 - \cos(2\pi t/T_H)], t \in [0, T_H]$$

The number of counts, N_B , in the tone bursts matches the length of the Hanning window, i.e., $T_H = N_B/f$.

The tone burst excitation was chosen in order to excite coherent single-frequency waves. This aspect is very important especially when dealing with dispersive waves (flexure, Rayleigh, Lamb, Love, etc). The Hanning window smoothing was applied to reduce the excitation of frequency side lobes associated with the sharp transition at the start and the end of a conventional tone burst. Two forms of the elastic wave propagation were studied: the axial waves and the flexural waves. We applied function-generated load of force and moment to the nodes delimiting the contour of these active areas. Consistent with the physical phenomenon, the force applied to nodes representing opposite ends of the piezoelectric wafer had to be in opposite phase. This ensures that the net effect on the structure is self-equilibrating. To generate axial waves, we applied force on the nodes. While for flexural waves, we applied moments. The detection of the elastic waves followed the same general principle as that applied to wave generation. The variables of interest were the differences between the displacements at the opposing ends of the active sensor, i.e.,

delta displacement for axial waves, and delta rotation for flexural waves. Figure 12a shows FEM simulation of axial waves signal received at sensors A–E when the beam was excited with a 100 kHz five-count Hanning-windowed axial burst at the left-hand end of the beam. It is easily appreciated how the wave travels down the beam from A to E, then reflects at the right-hand end, and returns to A, followed by repetition of this pattern. We observe that, at the beginning, the five counts of the smoothed tone-burst excitation can be readily identified. As the wave travels further and undergoes reflections, its coherence somehow diminishes, and some dispersion occurs. This loss of coherence may also be attributed to accumulation of numerical error. Flexural wave was also simulated with a 100 KHz five-count Hanning-windowed axial burst at the left-hand end as shown in Figure 12b. We note that the two burst wave packages were apparent in the wave form and that’s due to the reflection of the incident wave at the left-hand end of the beam. We observe that the flexural wave speed is roughly half of that of axial wave, since for the same distance; the flexural took roughly twice the traveling time.

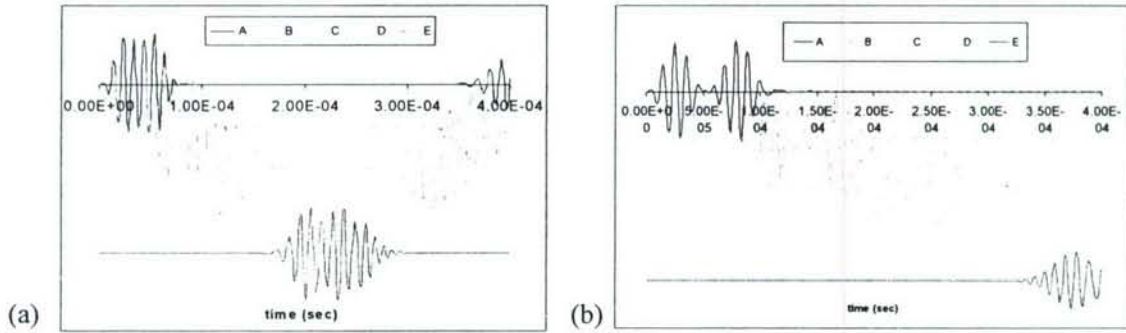


Figure 12 FEM simulation signals received at sensor A-E (100KHz five count smoothed tone-burst excitation at active sensor A). (a) axial wave; (b) flexural wave

Figure 13 shows the FEM simulation of the pulse-echo method used for crack detection. The active sensor placed at the left-hand end was used to send a 100 kHz five-count Hanning-windowed axial burst and to receive the elastic wave responses. Three situations: no crack, 2 mm crack and 6 mm crack were presented. In a beam without crack, the initial signal and the reflection from the right-hand end appear. If a 2 mm through-the-thickness transverse crack is simulated in the center of the beam, the reflection (echo) from this crack also appears but the amplitude of reflection was quite small, when the crack length increases from 2 mm to 6 mm, the amplitude of the reflection increases significantly. Figure 13b shows the FEM simulation of the pulse-echo method used for crack detection with flexural wave. Three situations: no crack, 2 mm crack and 6 mm crack were presented. In a beam without crack, the initial signal and the reflection from the right-hand end appear. We could observe similar result as in the case of axial wave.

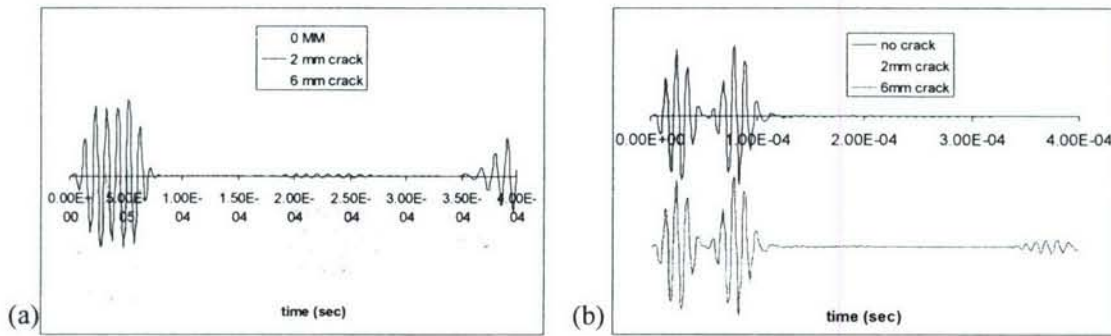


Figure 13 FEM simulation of pulse echo method. (a) axial wave; (b) flexural wave

2.3.2. COUPLED FIELD WAVE PROPAGATION SIMULATION

In previous analysis, waves were generated by applying force or moments on the beam, thus different modes of wave were separated and in some sense the real complex situation of wave composition and interaction were simplified, another issue is that the way to sense the wave motion, in the simulations we just discussed, pure structure response like relative displacement and rotation were used to analyze the structure response, while the piezoelectric effect of PWAS were not taken in account. To solve these issues, we will apply the coupled analysis on the structure, i.e., we will model PWAS directly with coupled field elements, excite the PWAS with electrical signals, and examine the electrical response of PWAS to the wave motion. Same beam with PWAS put at same positions were studied. The PWAS model were constructed with solid elements and attached on the beam model. Part of the specimen was shown in Figure 14. Bottom surface of the solid PWAS model was supposed to the beam surface and thus mechanical motion will be transferred between the two models. Similar five count tone burst was used to excite the structure. The difference here is that the excitation signals this time will be electrical voltage directly fed onto the top surface of the PWAS, simulating the operation as in real applications.

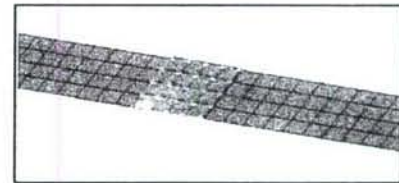


Figure 14 Mesh design of the beam and PWAS model

Similar simulation results were presented in Figure 15a and Figure 15b. Figure 15a shows the electrical signals receive at sensor A to sensor E as shown in Figure 11a. We could observe that because when the PWAS was excited by electrical signals, the generated wave will incorporate both axial mode and flexural mode, thus making the wave packet more complex than the signal excitation situation. We also simulate the effect of crack to the wave propagation. We put a 6mm crack at the symmetry line of the beam as in the previous analysis and record the electrical signals received at these PWAS. From Figure 15b we can see that the existence of the crack does affect the wave and echo from the crack could be

detected. Due to the page limitation, more details of the coupled field analysis will be discussed in future papers.

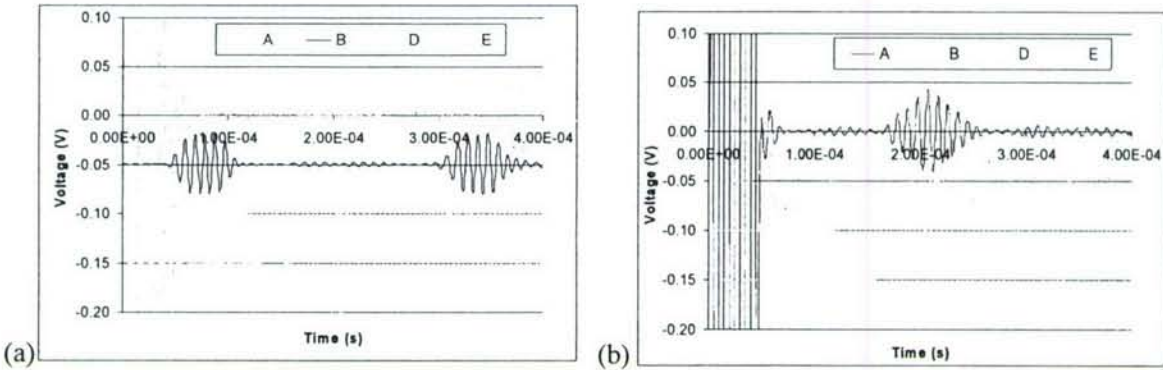


Figure 15 FEM simulation of pulse echo method. (a) axial wave; (b) flexural wave

3. SUPPORTING EXPERIMENTS FOR TASKS 1 AND 2

Experiments have been performed to validate the theoretical predictions and improve the theoretical model. The essential Lamb-wave dispersion curves, the energy spreading due to 2-D effects, and the Lamb-wave “sweet-spot” mode tuning effects have been measured. The transmitted and received power and energy for both continuous and tone-burst excitation have been determined. The in-situ PWAS immittance over a wide frequency range has been measured. Nonlinear saturation effects associated with signal amplitude and transmitted power have also been considered.

3.1. PWAS TUNING THEORETICAL AND EXPERIMENTAL RESULTS

The strain equations (1) and **Error! Reference source not found.** were coded into a Matlab program. The program gives the tuning curves of the structures for a given PWAS length, plate materials properties and thickness, and frequency range. Pitch-catch experiments were performed in which one PWAS served as Lamb waves transmitter and another PWAS served as receiver. The predicted values were compared with the experimental results. The signal used in the experiments was a Hanning-windowed tone burst with 3 counts. The signal was generated with a function generator (Hewlett Packard 33120A) and sent through an amplifier (Krohn-Hite model 7602) to the transmitter PWAS. A data acquisition instrument (Tektronix TDS5034B) was used to measure the signal measured by the receiver PWAS. Several plates were used in the experiments: (1) aluminum alloy 2024-T3 with 1.07 mm thickness and 1222 mm 1063 mm size; (2) aluminum alloy 6061-T8 with 3.15 mm thickness and 505 mm × 503 mm size; (3) aluminum alloy 2024-T3 with 3.15 mm thickness and 1209 mm × 1209 mm size . In each experiment, we used a pair of PWAS at a distance 250 mm from one another. One PWAS was used as transmitter and the other as receiver. The frequency of the signal was swept from 10 to 700 kHz in steps of 20 kHz. At each

frequency, we collected the wave amplitude and the time of flight for both the symmetric mode and the antisymmetric modes.

3.1.1. SQUARE PWAS

Square PWAS 7 mm long, 0.2 mm thick (American Piezo Ceramics APC-850) were used on two aluminum 2024-T3 plates of different thickness (1.07 mm and 3.15 mm) and one aluminum 6061-T8 plate of 3.15 mm thickness.

Experiments were conducted on 2024-T3 plate with 1.07 mm thickness and 1222 mm × 1063 mm size. In this experiment, PWAS were located at the center of the plate in order to avoid interference with the reflection from the boundaries. The group velocity of the S0 mode was detected with no difficulties at each frequency. The A0 mode was followed closely at each frequency, but, for frequencies where the wave amplitude was closer to zero, the experimental values were more distant from the predicted values. Figure 16a shows the experimental data of the wave amplitude for the S0 and A0 modes. Figure 16b shows the predicted values of the wave amplitude for the S0 and A0 modes for an effective PWAS length of 6.4 mm. For this effective PWAS length value, we obtain the best agreement between experiments and predictions. In the development of the theory, it was assumed that there was ideal bonding between the PWAS and the plate. This assumption means that the stresses between the transducers and the plate are fully transferred at the PWAS ends. In reality, the stresses are transferred over a region adjacent to the PWAS ends (Figure 1c). The experimental and theoretical values of the tuning are in good agreement (Figure 16). The first minimum of the A0 mode, both in the experimental graph and in the predicted graph, is found around 210 kHz. At this frequency, the S0 mode amplitude is nonzero and increasing. The theory also predicts the S0 maximum should happen at the same frequency as the second A0 maximum; this prediction was also verified by the experiments.

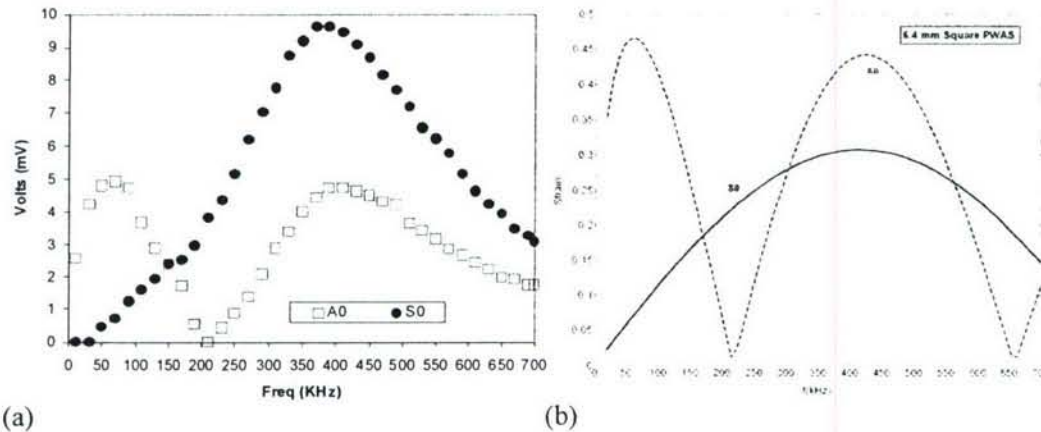


Figure 16 Square PWAS tuning: aluminum 2024-T3, 1.07 mm thickness, 7 mm square PWAS. (a) experimental data; (b) prediction with equation (1)

Experiments were also conducted on 2024-T3 plate with 3.15 mm thickness and 1209 mm × 1209 mm size. In this thicker plate, three Lamb wave modes (S0, A0, A1) exist in the testing frequency range. Figure 17 shows the group velocity for the S0, A0 and A1 modes. The experimental data is close to the predicted values for frequencies up to 550 kHz. Above this frequency, the group velocities of these three Lamb wave modes come into a common nexus. Hence, the three waves are too close and too dispersive to be measured accurately. In particular, it was found difficult to determine which wave represents the A0 mode and which represents the A1 mode. Figure 18a shows the experimental data of the amplitude of the A0, S0 wave, while Figure 18b shows the predicted values. The experimental and predicted values are in accordance up to 550 kHz. The S0 maximum is close to the A0 minimum at around 360 kHz. The A1 mode has also been detected.

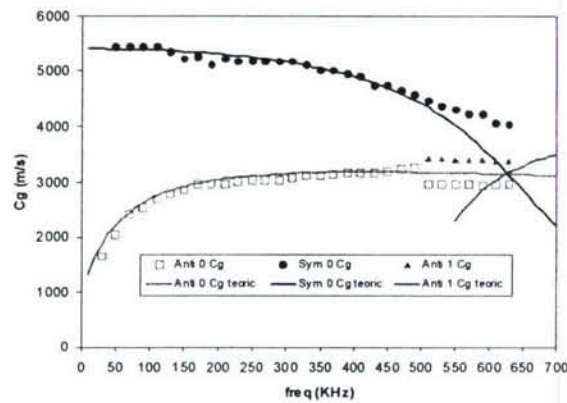


Figure 17 Group velocity: Aluminum 2024-T3, 3.15 mm thickness, 7 mm square PWAS

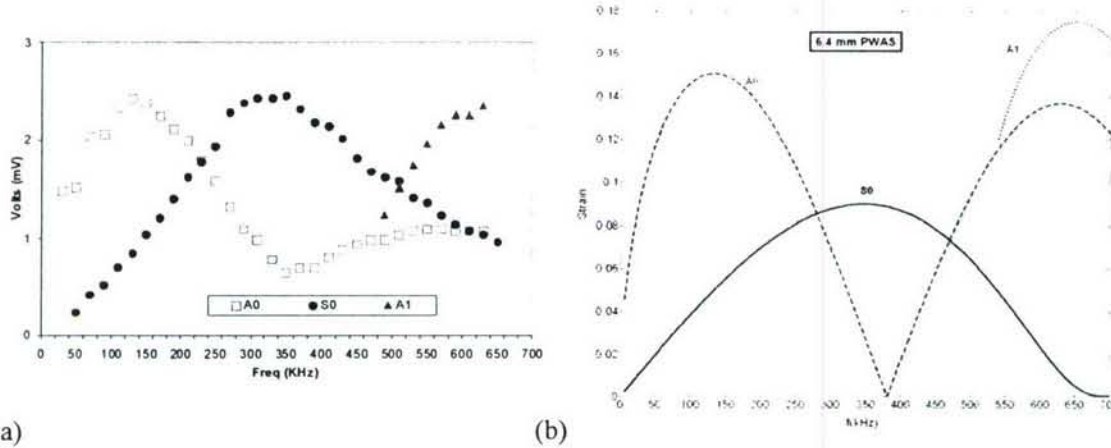


Figure 18 Square PWAS tuning: Aluminum 2024-T3, 3.15 mm thickness, 7 mm Square PWAS. (a) experimental data; (b) prediction with equation (1)

The last experiments were on 6061-T8 plate with 3.15 mm thickness and 505 mm x 503 mm size. The results were similar to those on the plate 1209 mm × 1209 mm, 3.15mm thick except for presence of

boundary reflections. The data followed the predicted values quite closely. At frequencies between 500 kHz and 700 kHz, both plates showed the presence of three modes, S_0 , A_0 , and A_1 . Figure 19 shows that at these high frequencies, their group velocities are close to each other and that both the S_0 mode and the A_1 mode are dispersive. The three wave packets are close to each other and a superposition effect starts to manifest, e.g., the tail of one wave packet interferes with the head of the next one. This superposition forms apparent decreases and increases of the actual packet amplitude. For example, Figure 19 shows the three wave packets at two different frequencies, 450 kHz and 570 kHz. At 450 kHz, it is possible to determine the location and amplitude of the S_0 mode while the superposition effect of the S_0 tail with the A_0 and A_1 modes makes it difficult to determine the location and amplitude of the A_0 and A_1 waves. At 550 kHz, it is possible to determine the location and amplitude of S_0 and that of a second wave, which could be either the A_0 or the A_1 mode. The distinction between A_0 and A_1 modes is difficult to determine, because it is difficult to follow their progression along the dispersion curves during the change of frequency. The third wave location and amplitude is approximate because the tails of the two other modes superpose with the third mode.

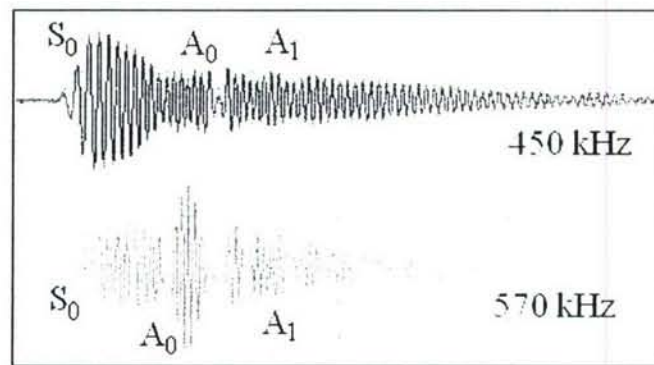


Figure 19 Wave propagation from the Oscilloscope at 450 kHz and 570 kHz

The effects described above were even more pronounced in the small plate of size 504 mm \times 501 mm. Above 450 kHz, it was difficult to locate the three waves, and the collected data seemed to be more distant from the predicted values. Moreover, the signal was disturbed by the reflection from the boundaries. Figure 20 compares the wave propagation of a 250 kHz tone burst in two 3.15 mm thick plates of different sizes. The boundary effects were much more pronounced in the small plate, where the reflection from the boundary was already affecting the slower A_0 mode. At 570 kHz, the superposition of the waves and the presence of the boundary reflection in the small plate made it quite difficult to determine the location and amplitude of the three modes.

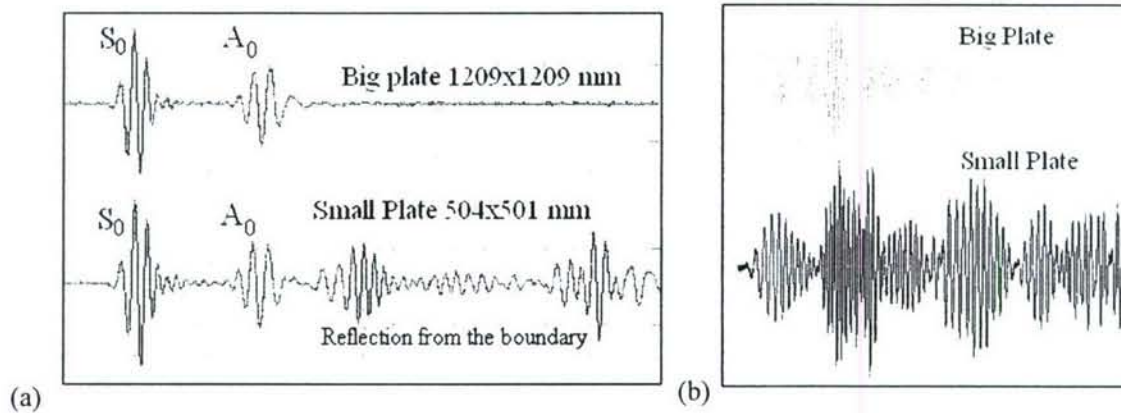


Figure 20 Waves propagation (a) 270 kHz: (b) 570 kHz

3.1.2. ROUND PWAS

Experiments with round PWAS diameter 7 mm, 0.2 mm thick (American Piezo Ceramics APC-850) were performed on two aluminum 2024-T3 plates of different thickness (1.07 mm and 3.15 mm). The results were found to be quite similar to those for square PWAS and, for sake of brevity, will not be reported here.

3.1.3. RECTANGULAR PWAS

Rectangular PWAS of high aspect ratio were tested to examine the directional tuning of Lamb waves. Three rectangular PWAS of 25 mm × 5 mm size, and 0.15 mm thickness (Steiner & Martin) were used. The experiment configuration is shown in Figure 21. PWAS P1 was the transmitter and PWAS P2 and P3 were the receivers. Two experiments are reported: PWAS P1 - P2; PWAS P1 - P3.

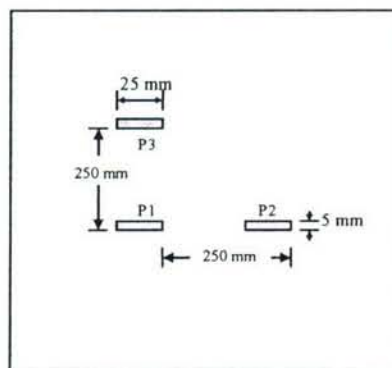


Figure 21 Aluminum plate 2024-T3 1.07 mm thick with rectangular PWAS

- (1) Transmitter P1, receiver P2

Figure 22a shows the experimental and predicted group velocity values. The A0 mode has been detected

well for frequencies below 400 kHz. The S0 mode shows a dispersion behavior in the experimental data at low frequency. The experimental data of the tuning is quite different from the predicted values (Figure 22b and Figure 23b). For the transmission from P1 to P2 the amplitude of the signal was very low compared with that of the other experiments. A new experiment was conducted sweeping the frequency from 25 kHz to 250 kHz at steps of 3 kHz. The intent of the new experiment was to visualize the three jumps of the A0 mode as shown in Figure 23b. Figure 23a shows the experimental values of the wave amplitude for frequency up to 250 kHz taken with steps of 3 kHz. The small steps we used to collect the data let us to detect the three maximum in the A0 mode that were not visible in the graph. The first two maxima are in accordance with the predicted values, while the third is at a higher frequency than that predicted. The S0 maximum is in accordance with the predicted values (Figure 23b). The value of the theoretical PWAS that best predicts the experimental behavior is 24.8 mm. It is interesting to note that when the receiver is along the line of the bigger dimension of the transmitter, the PWAS behaves as a square PWAS 25x25 mm long.

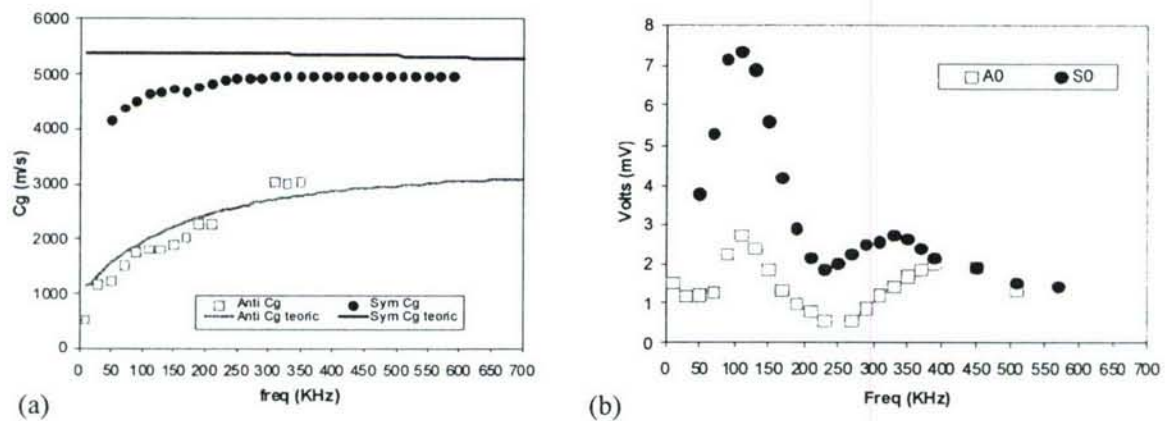


Figure 22 Plate 2024-T3, 1.07 mm thickness. Rectangular PWAS (P1-P2). (a) Group velocity; (b) Experimental data

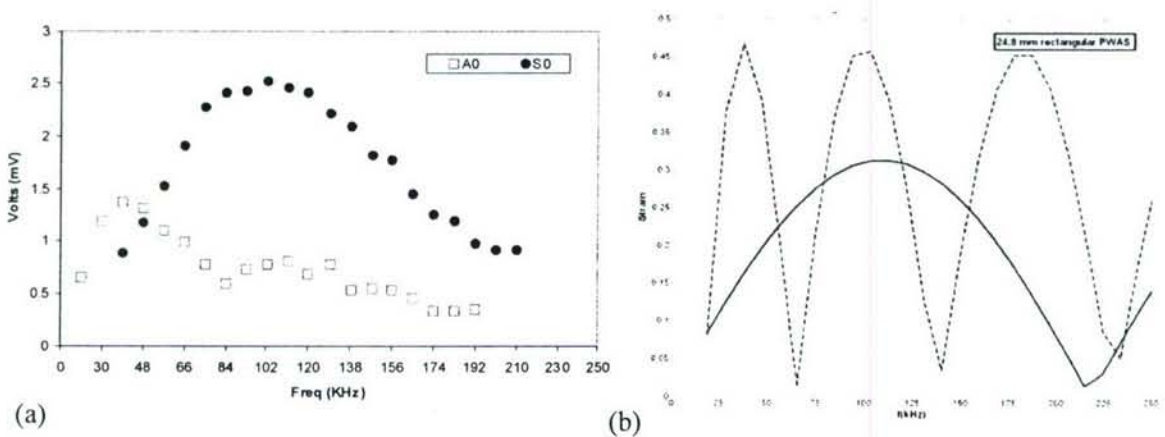


Figure 23 Plate 2024-T3, 1.07 mm thickness. Rectangular PWAS (P1-P2). (a) experimental data; (b) prediction data

(2) Transmitter P1, receiver P3

Figure 24a shows the experimental and predicted group velocity values with P1 as transmitter and P3 as receiver. A0 and S0 modes were detected well. The A0 mode location was hard to determine in the frequency over 300 kHz. Figure 24b shows the experimental values of the wave amplitude for the A0 and S0 modes. Both the A0 minimum and the A0 maximum are in accordance with the predicted values. The S0 mode has one maximum in both Figure 24b and Figure 25 but their location are different. Regarding the tuning, the predicted values were useful in detecting the frequency range to be used. The value of the theoretical PWAS that best predicts the experimental behavior seemed to be 4.5 mm.

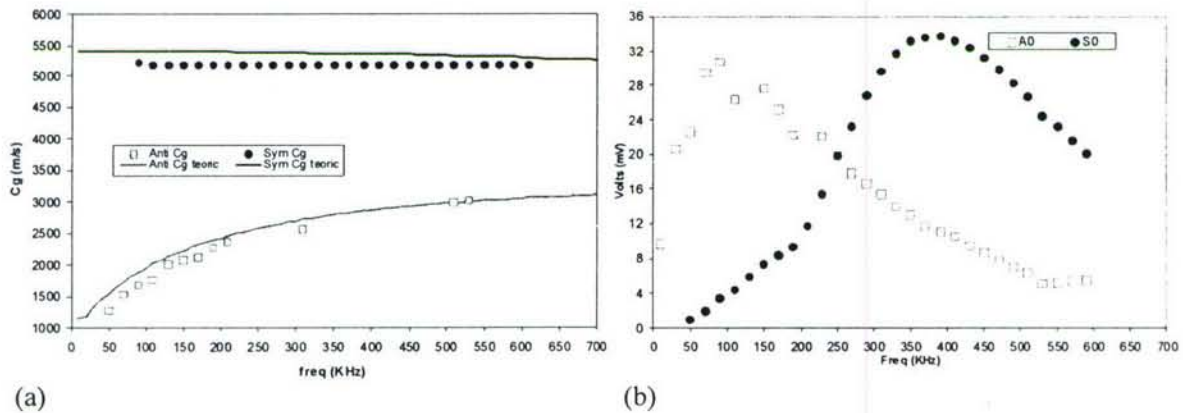


Figure 24 Plate 2024-T3, 1.07 mm thickness; rectangular PWAS (P1-P3). (a) Group velocity; (b) Experimental data

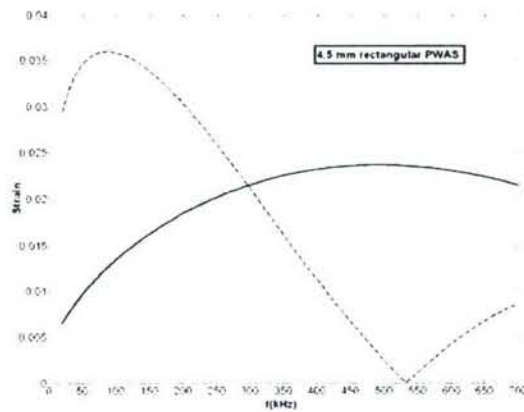


Figure 25 Tuning on plate 2024-T3, 1.07 mm thick; rectangular PWAS (P1-P3). Prediction with equation (1)

Table 1 Actual and effective PWAS length

Real PWAS length	Effective PWAS length	% of effective PWAS	% of non effective PWAS
25 mm	24.8 mm	99.2%	0.8%
7 mm	6.4 mm	91.4%	8.6%
5 mm	4.5 mm	90%	10%

3.2. PWAS TUNING APPLICATIONS

This section shows that the capability to excite only one desired Lamb wave mode is critical for practical applications such as PWAS phased array technique and the time reversal process. In PWAS phased array applications, the assumption of the presence of a single low-dispersion Lamb wave mode (S0) is invoked. Since several Lamb wave modes traveling at different speeds would disturb the damage imaging results. Examples are given of correctly tuned EUSR images vs. detuned cases, which illustrate the paramount importance of Lamb wave mode tuning. In the TRP study, an input wave packet is reconstructed at a transmission PWAS when the signal recorded at the receiving PWAS is reversed in the time domain and transmitted back to the original PWAS. Ideally, TRP could be used for damage detection without a prior baseline. However, the application of TRP to Lamb-waves SHM is impeded by the dispersive and multimodal nature of the Lamb waves. The presence of more than one mode usually produces additional wave packets on both sides of the original wave packet due to the coupling of the Lamb-wave modes. The PWAS Lamb-wave tuning technique described in this paper is used to resolve the side packets problem. Several tuning cases are illustrated. It is found that the 30 kHz tuning of the A0 Lamb-wave mode with a 16-count smoothed tone burst leads to the complete elimination of the side wave packets. However, the elimination was less perfect for the 290 kHz tuning of the S0 mode due to the frequency sidebands present in the tone-burst wave packet.

3.2.1. PWAS PHASED ARRAY APPLICATION

The concept of PWAS guided Lamb wave phased array utilizes an array of M closely spaced PWAS that are permanently attached to the structures and interrogate it at will (Giurgiutiu and Bao 2004). The wave pattern generated by the phased array is the result of the superposition of the waves generated by each individual element. By sequentially firing the individual elements of an array transducer at slightly different times, the ultrasonic wave front can be focused or steered in a specific direction. Thus, sweeping and/or refocusing of the beam is achieved electronically without physically manipulating the transducers.

As discussed earlier, Lamb waves can exist in a number of dispersive modes that can simultaneously exist at any given frequency. However, through smoothed tone-burst excitation of carrier frequency f_c and

frequency tuning, it is possible to confine the excitation to a particular Lamb wave mode, of wave speed c , and wave length λ/f_c . Consider for example the structural health monitoring of a thin-wall structure using Lamb waves. For a 1-mm wall thickness and an operation frequency range of 0-1000 kHz, two Lamb wave modes (A0 and S0) exist simultaneously. However, there are frequency values where one of the two modes is nearly suppressed. For example, for a 7-mm square PWAS at very low frequency (5 to 100 kHz), S0 mode vibration is very small and the A0 mode dominates (Figure 26a). Similarly, at frequency 210 kHz, S0 dominates and A0 barely exist. Group velocity frequency plots of S0 and A0 modes are shown in Figure 26b. We can see that within the 0~1000 kHz range, the S0 mode velocity is almost constant, i.e., the S0 mode is much less dispersive compared to the A0 mode. This observation is consistent with the fact that, usually in Lamb wave NDE/SHM applications, A0 mode is used for the detection of surface defects and disbonds/delaminations while S0 mode is used for through the thickness damage detection. Therefore, for crack detection using PWAS phased array, the S0 mode excitation is expected to give much better results. In addition, to obtain a high quality EUSR scanning image, we also need the response of the S0 Lamb wave mode to be sufficiently strong, thus carrying well the information about damage location and size. Another factor to be concerned during the frequency tuning is the ratio of d/λ . Our previous research has found out that this ratio should be smaller than or equal to 0.5 in order to observe the sampling theorem (otherwise a disturbing lobe called grating lobe may present). While within the effective range, larger d/λ value is desired since it offers better directivity, known as thinner mainlobe width. Scanning with a phased array having good directivity will give a more correct indication of the crack size. Due to the relation $\lambda=c/f$, we see that higher tuning frequency should be used for larger d/λ values. Therefore, the objective of frequency tuning applied to the PWAS phased arrays is to find an excitation frequency high enough and at which the response signal will have high S0/A0 ratio (in terms of magnitude) as well as high signal-noise-ratio (SNR) while observing the sampling theorem.

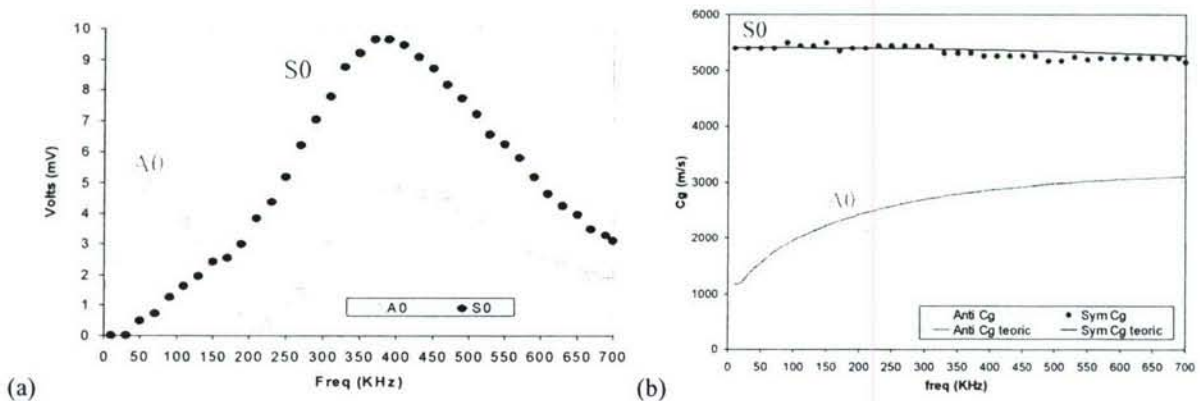


Figure 26 Frequency tuning for crack detection in a 1 mm thick aluminum plate specimen. (a) strain-frequency plot; (b) group velocity-frequency plot

The specimen used in the experiments was a 1220 mm square 1-mm thick panel of 2024-T3 Al-clad aircraft grade sheet metal stock. The crack is placed on a line midway between the center of the plate and its upper edge. The crack is 19 mm long, 0.127 mm wide. The crack is placed at broadside w.r.t. the phase array at coordinates (0, 0.305 m), i.e., at $r=305$ mm, $\phi_0=90^\circ$ (Figure 27a). The PWAS phased array was placed on a straight line in the center of the plate. During the Lamb-wave tuning procedure, both pitch-catch and pulse-echo methods were employed to find out the best tuning frequencies. The experimental voltage measurement obtained from pitch catch experiment is shown in Figure 27b. After tuning, EUSR experiments are conducted at the tuning frequency 300 kHz and as well at 450 kHz for understanding the significance of frequency tuning. EUSR scanning image results are shown in Figure 28.

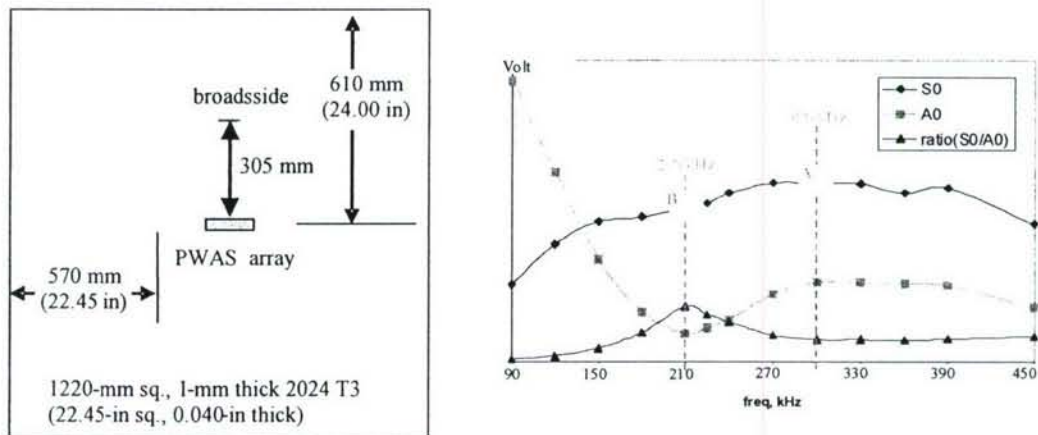


Figure 27 PWAS mode tuning for phased array application. (a) specimen layout; (b) experimental tuning curves

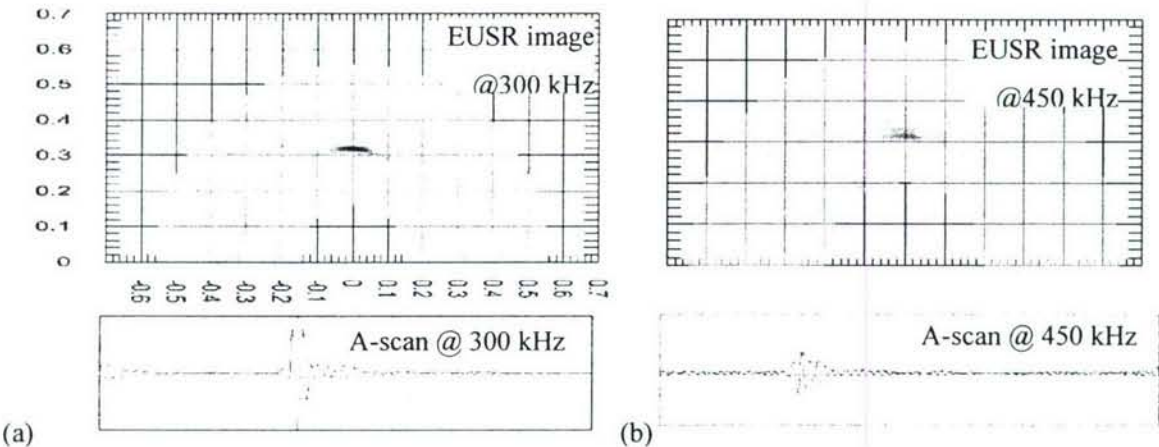


Figure 28 EUSR inspection using frequency tuning. (a) EUSR mapped image at 300 kHz tuning frequency; (b) EUSR image at 450 kHz

3.2.2. TIME REVERSAL METHOD

Time reversal invariance of the acoustic wave equations means that, for every burst of sound diverging from a source—and possibly reflected, refracted, or scattered by any propagation medium—there exists, in theory, a set of waves that precisely retrace all of these complex paths and converges in synchrony, at the original source, as if time were progressing backward. In this section, we will show that this effect (which hinders the use of time reversal procedure with Lamb-wave SHM) can be alleviated through the Lamb-wave tuning method discovered in this project.

Computations are first processed in frequency domain to calculate input signal V_{in} and structure transfer function $G(\omega)$, for discrete values of ω . In the second step, an inverse Fourier transform is performed to derive the dispersed forward wave V_x in time domain. Next, this forward wave is time reversed and denoted as signal V_y . Lastly, repeat first two steps but replace V_{in} with V_y , the input signal is reconstructed as V_{out} . If V_{in} is symmetric, V_{out} is in phase with V_{in} . If V_{in} is asymmetric, V_{out} should be time reversed to be in phase with V_{in} . The relationship between V_{out} and V_{in} is governed by the following equation:

$$V_{out}(t) = IFFT\{Y(\omega) \cdot G(\omega)\} = IFFT\{V_{in}(-\omega) \cdot |G(\omega)|^2\} \quad (23)$$

where $IFFT\{\}$ denotes inverse Fourier transform, time-reversal property of Fourier transform was used in the deduction. Note that $|G(\omega)|^2$ is the frequency-dependent transfer function that affects the wave propagation through the medium.

For Lamb waves with only two modes (A0 and S0) excited, the $G(\omega)$ function can be written as

$$G(\omega) = S(\omega)e^{-i\xi^S x} + A(\omega)e^{-i\xi^A x} \quad (24)$$

where $S(\omega) = -i \frac{\alpha \tau_0}{\mu} \sin(\xi^S a) N_S(\xi^S) / D_S'(\xi^S)$, $A(\omega) = -i \frac{\alpha \tau_0}{\mu} \sin(\xi^A a) N_A(\xi^A) / D_A'(\xi^A)$, $\xi = \omega/c$, c represents the phase velocity. Thus,

$$|G(\omega)|^2 = |S(\omega)|^2 + |A(\omega)|^2 + S(\omega)A^*(\omega)e^{-i(\xi^S - \xi^A)x} + S^*(\omega)A(\omega)e^{i(\xi^S - \xi^A)x} \quad (25)$$

where $*$ denotes complex conjugate, and $|S(\omega)|^2$, $|A(\omega)|^2$ are a series of real numbers. Substitute Eq. (25) into Eq. (23), the first and the second terms on the R.H.S. of Eq. (25) will introduce together one wave packet at the excitation point, while the third and fourth terms will introduce two extra wave packets in the reconstructed wave V_{out} in time domain respectively.

The positions of these extra wave packets can be predicted using Fourier transform property of right/left shift in time. Hence, for Lamb wave with two modes (S0 mode and A0 mode), the reconstructed wave V_{out} will contain three wave packets. The input signal is not fully reconstructed in this case. This

theoretical deduction explains the experimental observations of other researchers. However, this situation could be alleviated if single mode-Lamb wave could be excited. For single-mode Lamb wave (e.g., assume S0 mode is dominant after frequency tuning), $G(\omega)$ function can be written as

$$G(\omega) = S(\omega)e^{-i\epsilon^S x} \quad (26)$$

Thus, V_{out} in Eq. (23) has the same phase spectrum as the time-reversed V_{in} (if V_{in} is symmetric, time-reversed V_{in} is identical to V_{in}), and the magnitude spectrum of V_{out} equals the magnitude spectrum of V_{in} modulated with $|G(\omega)|^2$. For narrow-band excitation, $|G(\omega)|^2$ can be assumed to be constant. In this case, V_{out} contains one wave packet representing a perfect reconstruction of the input signal V_{in} . If $|G(\omega)|^2$ varies considerably in the excitation frequency band, the reconstructed signal V_{out} still contains one wave packet but may or may not have a similar shape of the input signal V_{in} .

We have shown in the previous section that, in order to fully reconstruct the input Lamb wave signal with the time reversal procedure, the input signal should be tuned to a frequency point where only one Lamb wave mode is dominant. To achieve this, a narrow-band input signal is always preferred. In our simulation, we considered two 6.4-mm round PWAS, one as transmitter and the other one as receiver, 400 mm apart on a 1 mm aluminum plate. Figure 29 shows the normalized strain plots of Lamb-wave A0 mode and S0 mode of a 1mm aluminum plate. Note that the strains of two Lamb wave modes are frequency-dependent.

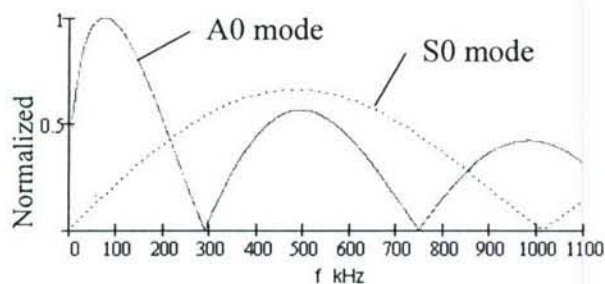


Figure 29 Predicted Lamb wave response of a 1-mm aluminum plate under PWAS excitation: normalized strain response for a 7-mm round PWAS (6.4 mm equivalent length)

A number of narrow-band tone bursts (16-count Hanning windowed) of different carrier frequencies were tested and the input signal was reconstructed using the time-reversal method. Figure 30, Figure 31 and Figure 32 show the reconstructed waves and residual waves obtained after applying the time reversal method. The input signals were 16-count tone bursts with 500 kHz, 290 kHz and 30 kHz carrier frequency, respectively. The first frequency corresponds to a case in which both the A0 and the S0 modes are excited. The second frequency corresponds to a preferential excitation (tuning) of the S0 mode, whereas the third frequency corresponds to the preferential excitation (tuning) of the A0 mode. These

three cases are discussed in detail next. As indicated in Figure 29, A0 mode and S0 mode show similar strength around 500 kHz. Therefore, both wave modes are excited by the 500 kHz tone burst. Subsequently, the time-reversed reconstructed wave (Figure 30) displays two big residual wave packets to the left and right of the reconstructed wave. This is exactly the case observed experimentally by [13]. In contrast, as indicated by Figure 29, the 290 kHz frequency generates a tuning of the S0 mode. When the S0 mode is dominant, the reconstructed waveform is getting much better with much smaller residual packets. However, as shown in Figure 31, there are still some small residual wave packets, to the left and to the right of the main reconstructed wave. The reason for these residual wave packets is that the 16-count tone burst has a finite bandwidth, and hence a small amplitude residual A0 mode gets excited besides the dominant S0 mode. To eliminate the residual waves, a tone burst with increased count number, i.e., narrower bandwidth, should be used. However, the signal will become long in time duration and lost its resolution in time domain. If we excite with a low frequency, such as 30 kHz, we find from Figure 29 that the A0 mode is dominant while the S0 mode is very weak. In addition, at these lower frequencies, the bandwidth of the 16-count tone burst input signal becomes narrower in actual kHz values as compared with the high-frequency bands. Hence, as indicated in Figure 32, the 30 kHz test signal resulted in a very good reconstruction with the time-reversal method. We see from Figure 32, that the A0 mode dominates and that the narrow-band input signal was perfectly reconstructed by the time-reversal method, with practically no residual wave packets being observed.

Another important fact studied in our simulation was the relative amplitude of the reconstructed wave and the residual wave packets obtained during the time-reversal process at various excitation frequencies. Figure 33 shows the plots of the reconstructed wave packet amplitude and of the residual wave packets amplitudes over a wide frequency range (10 kHz ~ 1100 kHz). As it can be seen, for an input signal with fixed number of counts (here, a 16-count tone burst), the residual wave packets amplitudes vary with respect to input signal tuning frequency. The residual reaches local minimum values and local maximum values at certain tuning frequency points. Hence, frequency tuning technique can be used to select the optimized input signal frequency that will improve the reconstruction of the Lamb wave input signal with the time-reversal procedure, thus giving a much cleaner indication of damage presence, when damage in the structure is detected through the break down of the time reversal process. For example, for the PWAS size of 7mm and plate thickness of 1mm considered in our simulation. Figure 33 indicates that, the 30 kHz, the 300 kHz, the 750 kHz, and probably the 1010 kHz would be optimal excitation frequencies to be used with the time reversal damage detection procedure for this particular specimen and PWAS types.

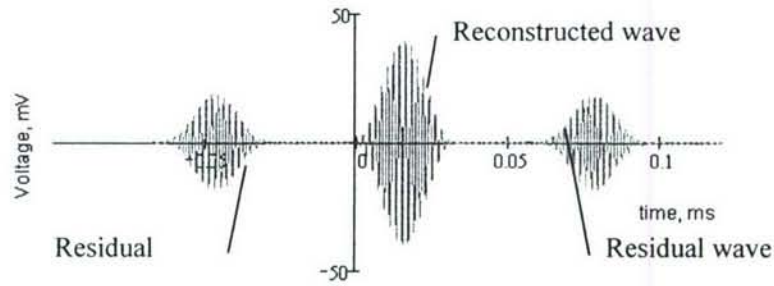


Figure 30 Untuned time reversal: reconstructed input using 16-count tone burst with 500k Hz carrier frequency; strong residual signals due to multimode Lamb waves are present.

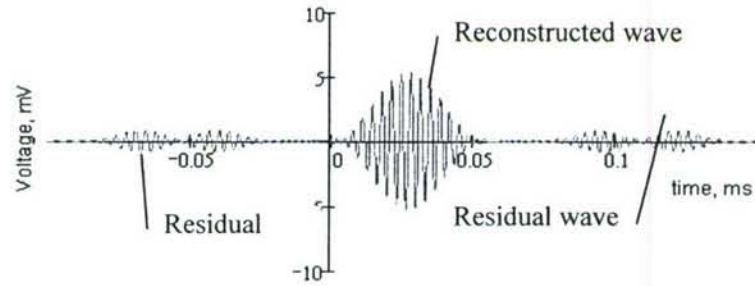


Figure 31 Time reversal with S0 Lamb wave mode tuning : reconstructed input using 16-count tone burst with 290 kHz carrier frequency; weak residual wave packets due to residual A0 mode component are still present due to the side band frequencies present in the tone burst

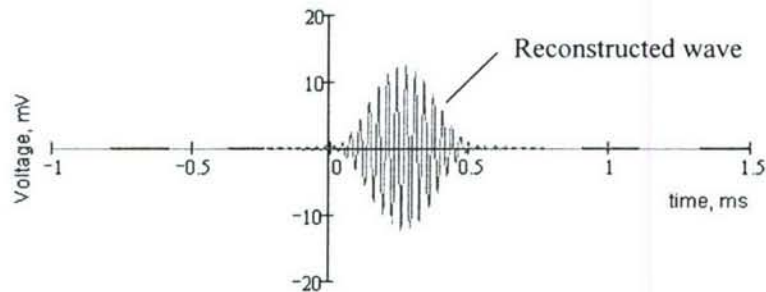


Figure 32 Time reversal with A0 Lamb mode tuning: reconstructed input using 16-count tone burst with 30 kHz carrier frequency; no residual wave packets are present

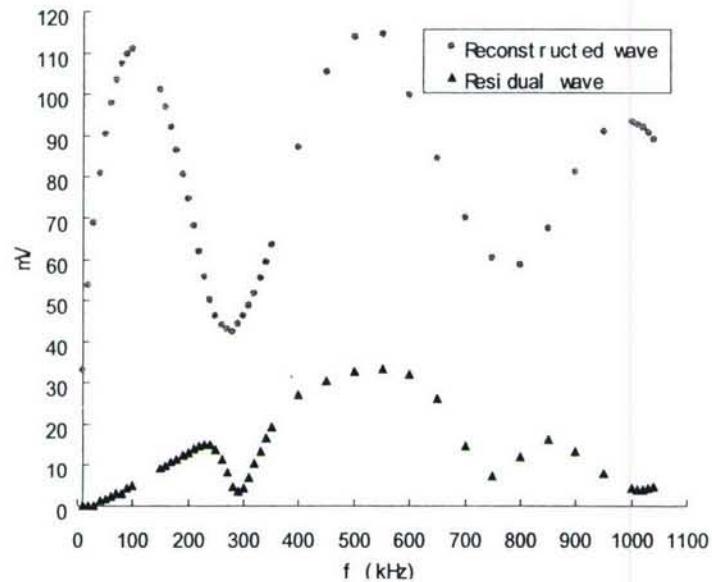


Figure 33 Reconstructed wave and residual wave in terms of their maximum amplitudes using 16-count tone burst over wide frequency range (10 kHz ~ 1100 kHz)

4. WORK BEYOND THE ORIGINAL PROPOSAL

This project has resolved fundamental aspects of PWAS interaction with metallic structures and develops methods to maximize PWAS effectiveness in embedded ultrasonic NDE of metallic structures. These results are valuable for the structural health monitoring of the Air Force’s aging aircraft fleet, which raises most of the present-day maintenance problems. We have extended the present analysis to address the following issues.

4.1. IN-SITU FABRICATED SMART MATERIALS ACTIVE SENSOR

The focus of this investigation is to investigate alternate ways of creating PWAS that have better properties and durability than those currently employed. One way is that of in-situ PWAS fabrication using composite fabrication techniques. The piezoelectric composites have the advantage that electric signals can be collected directly, whereas in the case of piezomagnetic composites magnetic flux probes had to be used. Our purpose in pursuing the fabrication of piezoelectric composites was to eventually be able to achieve in-situ fabrication of PWAS of a quality comparable with that of ceramic PWAS. By fabricating the PWAS directly onto the structure a seamless bond would be achieved between the PWAS and the structure that would be impervious to environmental attacks can be created. Thus, we will eliminate the “weak link” in the present use of bonded PWAS and achieve a long time durability of the embedded sensory system.

4.1.1. PREPARATION AND FABRICATION

The epoxy resin used in the fabrication of the piezoelectric composite PWAS was EPO-TEK 301-2 from Epoxy Technology, Inc. This epoxy has a good handling property, high dielectric strength and a low viscosity. The mixture ratio for the epoxy part “A” and part “B” (hardener) is specified as 1: 0.35 by the supplier and was followed in this study. The PZT particles in the composite PWAS were PZT-5B powders from Morgan Electro Ceramics. PZT-5B powders have a high sensitivity and high time stability (Figure 34). The silver paint used for creating the electrodes was acquired from SPI Supplies and Structure Probe, Inc. The poling workstation consists of an oven, a constant DC power supply, a high voltage power supply, a multimeter and a thermometer.

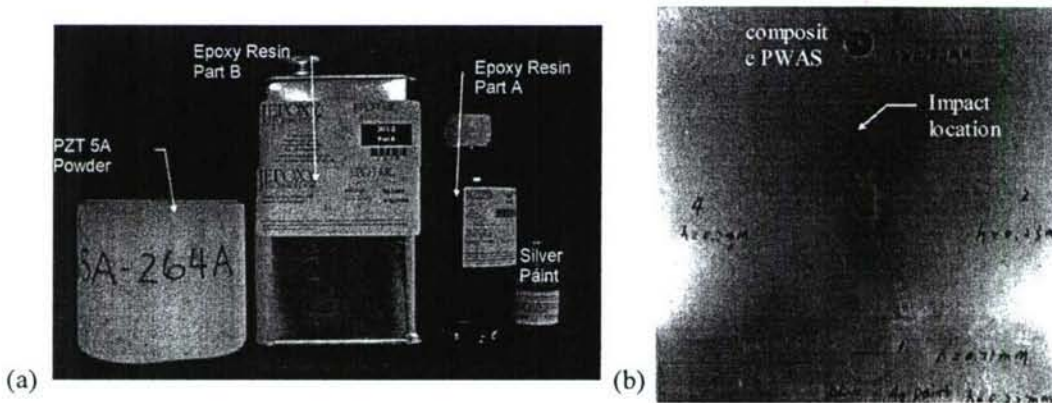


Figure 34 Composite PWAS experiments: materials used; (b) Composite PWAS sample fabricated on a thin aluminum plate was used in measuring the impact waves

Then the surface of host structure was cleaned and put a mask. The mask has a 7mm diameter, 0.2mm thickness hole and its center is in the desired position. PZT powder with a weight fraction of 85% was added to the epoxy matrix phase and was stirred thoroughly. The paste was then spread into the mask and let it cure at an elevated temperature (50 degree C) until hard. Remove excess and sand it down to final thickness. A small piece of copper foil was applied to one side of the cured composite PWAS to form an electrode. After curing and electroding had been completed, poling of the composite PWAS was subsequently carried out to activate its piezoelectric effect. A constant DC voltage of 1 kV was applied to the composite PWAS to pole the sample for four hours at 80 degree C.

4.1.2. CHARACTERIZATION AND IMPACT TEST

We measured the final size of the composite PWAS. It is 7mm diameter and 0.2mm thickness which is same as the traditional PWAS. The electricity of the composite PWAS was measured before and after poling. The resistance is greater than 40 M Ω before and after poling. The resistivity is higher than 40 M Ω m. The capacitance of composite is only 0.02nF which is lower than the traditional PWAS value 3nF.

The effectiveness of the composite PWAS for impact was investigated based on an impact test setup shown in Figure 34b. Impact point shown in the Figure 34b and it is 20mm away from the center of the composite PWAS. The output of the composite PWAS was measured simply as a voltage signal using a digital oscilloscope. We measured the voltage signal before and after poling (Figure 35). Before poling, the voltage signal damped out very soon. After poling, we can find the voltage amplitude is much higher than that before poling. And it also shows some vibration signal after the impact. From this figure, it is seen that upon hit, the beam vibrated first and then slowly damped out. The composite PWAS have a good repeatability in its output signal when subjected to similar impact forces.

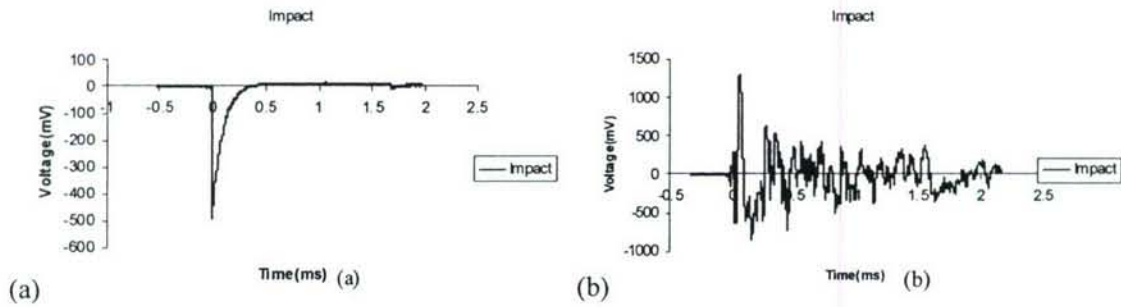


Figure 35 electric voltage signal measured by the impact hammer, (a) before poling (b) after poling

4.2. PWAS LAMB WAVE GENERATION ON COMPOSITE PLATES

4.2.1. PWAS LAMB WAVE DISPERSION CURVES

The test on composite specimens was performed to derive the probability of detection curves for PWAS Lamb wave generation and detection on composite structures. A quasi-isotropic plate $[(0/45/90/-45)_{2s}]$ has been studied. The layer material is A534/AF252. From the theoretical analysis, it is possible to extract the first 3 modes of interest. Figure 36 shows the theoretical and experimental data curves. The theoretical and experimental data for the A0 mode are in quite good agreement; theoretical and experimental data for the SH and S0 modes are also in good correlation with each other for low frequencies. At higher frequencies, where the two waves are closer, it is difficult to determine experimentally the wave location due to their superposition and dispersion.

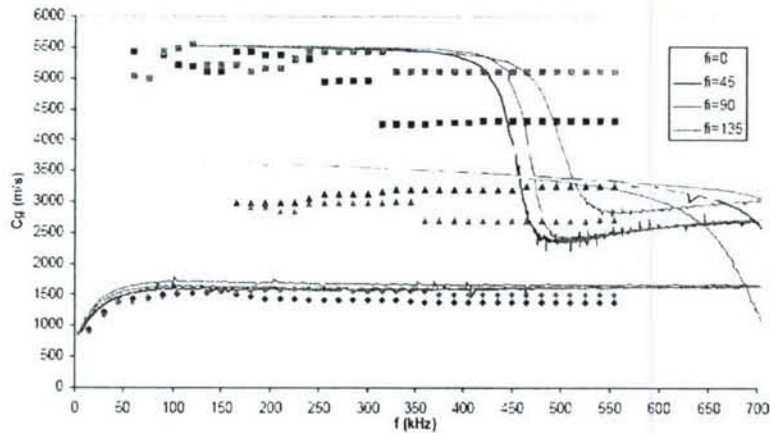


Figure 36 Group velocities for a quasi-isotropic plate using theoretical values (solid lines) and experimental values (dot lines)

4.2.2. PWAS LAMB WAVE TUNING

Pitch-catch experiments were performed on a composite plate in which one PWAS served as transmitter and another PWAS served as receiver. Specimen layout is shown in Figure 37a. The data received by PWAS #3 on 90° fiber direction were analyzed. Clay dam was used around the boundary to attenuate the boundary reflections. During the experiments two modes were detected, S0 and A0 modes. The SH0 mode was not possible to be located. The experiments were performed without an amplifier. The S0 amplitude was always quite low and at frequency above 140 kHz, the wave amplitude was of the order of magnitude of the noise. Figure 37b shows the experimental data. Normal mode expansion theory was used to derive the theoretical prediction of the tuning curves. Both A0 and S0 modes were scaled of the same amount to compare them to the experimental data. The A0 mode tuning curve predicts the frequency at which the A0 amplitude reaches a maximum with good accuracy. For the S0 mode, however, the theoretical and experimental results are not in agreement.

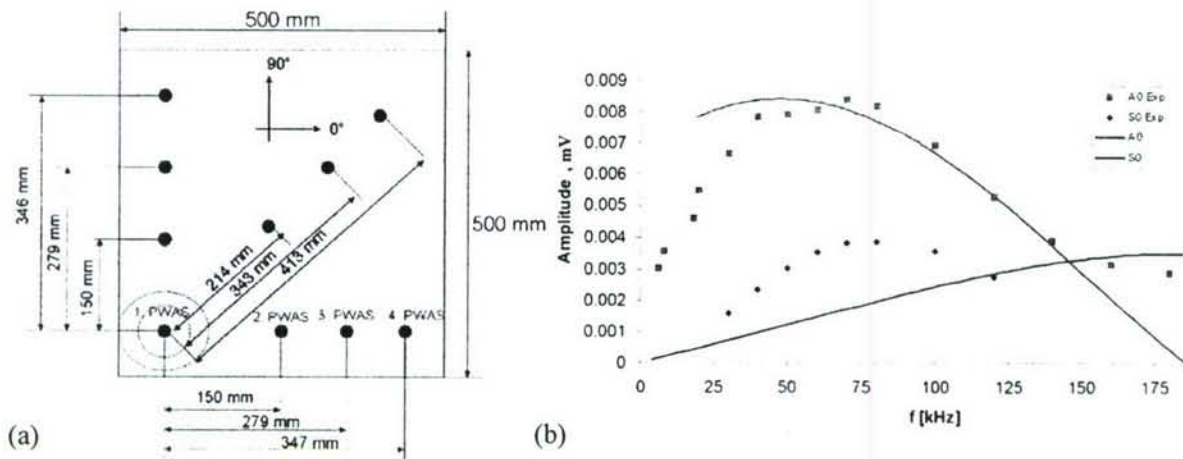


Figure 37 PWAS Lamb wave tuning on composite plate (solid line – theoretical results; dot line – experimental results)

REFERENCES

- Raghavan A., Cesnik C. E. S. (2004) "Modeling of piezoelectric-based Lamb-wave generation and sensing for structural health monitoring"; Proceedings of SPIE - Volume 5391 Smart Structures and Materials 2004: Sensors and Smart Structures Technologies for Civil, Mechanical, and Aerospace Systems, Shih-Chi Liu, Editor, July 2004, pp. 419-430

SIGNIFICANCE OF THE ACCOMPLISHMENTS

The emerging field of embedded ultrasonic NDE has the potential to produce fundamental changes in structural health monitoring, damage detection, and non-destructive evaluation by using small inexpensive and unobtrusive transducers that are permanently attached to the structure and can be interrogated at will. Piezoelectric wafer active sensors (PWAS) are the enabling technology for implementing embedded ultrasonic NDE. PWAS are about the only transducers that can be embedded in large numbers in the structure without extensive cost and weight penalty. In this funded research, the fundamental aspects of the PWAS-structure interaction have been intensively studied and verified based on experimental explorations. The PWAS Lamb wave tuning addressed the fundamental aspects of the interaction between PWAS and structure during embedded ultrasonic NDE, and also addressed a practical need and filled a gap in the modeling and analysis of this new technology. The project increased the understanding and generated the analysis\simulation tools for embedded ultrasonic NDE systems design. The outcomes are:

1. Comprehensive predictive model to explain how PWAS mounted on thin-wall structures excite and detect Lamb waves. Identify Lamb mode tuning conditions for maximum excitation/detection
2. Analysis of the in-situ PWAS immittance in interaction with Lamb waves traveling in the thin-wall structure

The predictive models developed in this project contribute to the design of embedded ultrasonic NDE networks that achieve maximum performance with minimum power consumption. The results of the funded project will advance the state of knowledge in the field of embedded ultrasonic NDE and will answer crucial questions. Particularly, we showed how PWAS Lamb wave tuning is significant to practical PWAS based SHM. We also demonstrated this technology's potential to an in-situ fabricate transducers and applications to composite structures health monitoring.

The results of the funded research will considerably expedite the implementation of structural health monitoring (SHM) into the aging Air Force fleet, and on future Air Force systems. PWAS-SHM will allow the maintainer to focus on critical areas and address repairs as needed rather than as scheduled. Thus, it will increase the safety and availability of the Air Force fleet, while reducing the operation and support costs.

PUBLICATIONS/PRESENTATIONS

- Cuc, A.; Giurgiutiu, V. (2006) "Propagation of Guided Lamb Waves in Bonded Specimens Using Piezoelectric Wafer Active Sensors", *SPIE's 13th International Symposium on Smart Structures and Materials and 11th International Symposium on NDE for Health Monitoring and Diagnostics*, San Diego, CA, 26 February–2 March, 2006, paper #6174-40
- Lin, B.; Giurgiutiu, V.; Yuan, Zh.; Liu, J.; Chen, Ch.; Bhalla, A.S.; Guo, R. (2007) "Ferroelectric Thin-Film Active Sensors for Structural Health Monitoring", *Proc. of SPIE Vol. 6529*, paper #6529-16
- Lin, B.; Giurgiutiu, V. (2005) "PVDF and PZT piezoelectric wafer active sensors for structural health monitoring", *Proceedings of the ASME IMECE Congress*, Nov. 5-11, 2005, Orlando, FL, paper #IMECE 2005-80400, CD-ROM
- Lin, B. and Giurgiutiu, V. (2006) "Modeling and Testing of PZT and PVDF Piezoelectric Wafer Active Sensors", *Smart Materials & Structure*, Vol. 15, 2006, pp 1085-1093
- Lin, B.; Giurgiutiu, V. (2005) "Review of In-situ Fabrication Methods of Piezoelectric Wafer Active Sensor for Sensing and Actuation Applications" *SPIE's 12th International Symposium on Smart Structures and Materials and 10th International Symposium on NDE for Health Monitoring and Diagnostics, Sensors and Smart Structures Technologies for Civil, Mechanical, and Aerospace Systems Conference*, 6-10 March 2005, San Diego, CA, paper # 5765-04
- Lin, B.; Giurgiutiu, V. (2006) "On the Modeling of Piezoelectric wafer active sensor impedance analysis for structural health monitoring", *SPIE's 13th International Symposium on Smart Structures and Materials and 11th International Symposium on NDE for Health Monitoring and Diagnostics*, San Diego, CA, 26 February–2 March, 2006, paper #6174-08
- Giurgiutiu, V. and Lin, B. (2004) "In-situ Fabricated Smart Material Active Sensors for Structural Health Monitoring", *SPIE AU04 International Symposium on Smart Materials, Nano-, and Micro-Smart Systems*, 12-15 December 2004, Conference AU101 Smart Materials III, Sydney, Australia
- Liu, W.; Giurgiutiu, V. (2005) "Automation of Data Collection for PWAS-based Structural Health Monitoring", *SPIE's 12th International Symposium on Smart Structures and Materials and 10th International Symposium on NDE for Health Monitoring and Diagnostics, Sensors and Smart Structures Technologies for Civil, Mechanical, and Aerospace Systems Conference*, 6-10 March 2005, San Diego, CA. paper # 5765-129
- Liu, W.; Giurgiutiu, V. (2005) "Signal Acquisition/Conditioning for Automated Data Collection during Structural Health Monitoring with Piezoelectric Wafer Active Sensors", *Proceedings of the 5th International Workshop on Structural Health Monitoring*, 11-14 September 2005, Stanford University, CA, pp. 606-618
- Liu, W.; Giurgiutiu, V. (2005) "Signal Acquisition/Conditioning for Automated Data Collection during Structural Health Monitoring with Piezoelectric Wafer Active Sensors", *2005 ASME International Mechanical Engineer Congress*, November 5-11, 2005, Orlando, Florida, paper #IMECE2005-79773
- Liu, W.; Giurgiutiu, V. (2006) "Finite element modeling and simulation of piezoelectric wafer active sensors interaction with the host structure for structural health monitoring", *SPIE's 13th International Symposium on*

- Smart Structures and Materials and 11th International Symposium on NDE for Health Monitoring and Diagnostics, San Diego, CA, 26 February–2 March, 2006, paper #6174-107
- Liu, W. and Giurgiutiu, V. (2007) “Finite Element Simulation of Piezoelectric Wafer Active Sensors for Structural Health Monitoring with Coupled-Field Elements”, Proc. of SPIE Vol. 6529, paper #6529-125
- Xu, B.; Giurgiutiu, V. (2006) “Development of DSP-based Electromechanical (E/M) Impedance Analyzer for Active Structural Health Monitoring” SPIE's 13th International Symposium on Smart Structures and Materials and 11th International Symposium on NDE for Health Monitoring and Diagnostics, San Diego, CA, 26 February–2 March, 2006, paper #6174-26
- Xu, B.; Giurgiutiu, V.; Crachiolo, G. (2006) “Development of Piezoelectric Oscillator Sensor for In-Vivo Monitoring of Capsule Formation around Soft Tissue Implants”, SPIE's 13th International Symposium on Smart Structures and Materials and 11th International Symposium on NDE for Health Monitoring
- Xu, B. and Giurgiutiu, V. (2007) “Lamb Waves Time-reversal Method Using Frequency Tuning Technique for Structural Health Monitoring”, Proc. of SPIE Vol. 6529, paper #6529-25
- Giurgiutiu, V.; Xu, B.; Cuc, A. (2005) “Dual Use of Traveling and Standing Lamb Waves for Structural Health Monitoring”, IMAC XXIII Conference & Exposition on Structural Dynamics, Orlando, Florida, January 31-February 3, 2005, paper # 361
- Giurgiutiu, V.; Xu, B.; Chao, Y.; Liu, S.; Gaddam, R. (2006) “Smart Sensors for Monitoring Crack Growth Under Fatigue Loading Conditions”, Journal of Smart Structures and Systems, Vol.2, No.2, pp.101-113
- Xu, B.; Giurgiutiu, V. (2005) “Efficient Electromechanical (E/M) Impedance Measuring Method for Active Sensor Structural Health Monitoring”, SPIE's 12th International Symposium on Smart Structures and Materials and 10th International Symposium on NDE for Health Monitoring and Diagnostics, Sensors and Smart Structures Technologies for Civil, Mechanical, and Aerospace Systems, San Diego, CA, 6-10 March, 2005, San Diego, CA, paper # 5765-30
- Bottai, G.; Giurgiutiu, V. (2005) “Simulation of the Lamb Wave Interaction between Piezoelectric Wafer Active Sensors and Host Structure”, SPIE's 12th International Symposium on Smart Structures and Materials and 10th International Symposium on NDE for Health Monitoring and Diagnostics, Sensors and Smart Structures Technologies for Civil, Mechanical, and Aerospace Systems Conference, San Diego, CA, 6-10 March 2005, San Diego, CA, paper # 5765-29
- Bottai, G.; Giurgiutiu, V. (2006) “Lamb Wave Tuning Between Piezoelectric Wafer Active Sensors and Host Structure: Experiments and Modeling”, Proceedings of IMECE2006, 2006 ASME International Mechanical Engineering Congress and Exposition, November 5-10, 2006, Chicago, Illinois, paper# IMECE2006-13533
- Santoni-Bottai, G.; Giurgiutiu, V. (2005) “Lamb wave interaction between piezoelectric wafer active sensors and host structure in a composite material”, Proceedings of the 5th International Workshop on Structural Health Monitoring, 11-14 September 2005, Stanford University, CA, pp. 1777-1784
- Santoni, G.B.; Yu, L.; Xu, B.; Giurgiutiu, V. (2007) “Lamb Wave Mode Tuning of Piezoelectric Wafer Active Sensors for Structural Health Monitoring”, Journal of Vibration and Acoustics, (Accepted), paper # VIB-06-1108

- Yu, L.; Giurgiutiu, V. (2007) "In-situ Optimized PWAS Phased Arrays for Lamb Wave Structural Health Monitoring", *Journal of Mechanics of Materials and Structures*, (Accepted), paper # 060720-Yu
- Yu, L. and Giurgiutiu, V. (2007) "Omnidirectional Guided Wave PWAS Phased Array for Thin-wall Structure Damage Detection", *Proc. of SPIE Vol. 6529*, paper #6529-107
- Yu, L.; Giurgiutiu, V. (2006) "Design, implementation, and comparison of guided wave phased arrays using embedded piezoelectric wafer active sensors for structural health monitoring", *SPIE's 13th International Symposium on Smart Structures and Materials and 11th International Symposium on NDE for Health Monitoring and Diagnostics*, San Diego, CA, 26 February–2 March, 2006, paper #6173-60
- Yu, L.; Giurgiutiu, V. (2005) "Multi-damage Detection with Embedded Ultrasonic Structural Radar Algorithm using Piezoelectric Wafer Active Sensors through Advanced Signal Processing", *SPIE's 12th International Symposium on Smart Structures and Materials and NDE for Health Monitoring and Diagnostics, Health Monitoring and Smart NDE of Structural and Biological Systems Conference*, 6-10 March, 2005, San Diego, CA, paper # 5768-48

INVENTION DISCLOSURE

Giurgiutiu, V. and Yu, L. (2006) "Optimized Embedded Ultrasonic Structural Radar (EUSR) System with Piezoelectric Wafer Active Sensors (PWAS) Phased Arrays for In-Situ Wide-Area Damage Detection during SHM and NDE", Invention Disclosure submitted to University of South Carolina, USCRF IDF No. 597

HONORS/AWARDS

Victor Giurgiutiu, PI (Feb. 15, 2004 to May 30, 2006):

1. Fellow of the American Society of Mechanical Engineers (ASME)
2. Fellow of Royal Aeronautical Society (RAeS)

INTERACTIONS/TRANSITIONS

The fundamental research results obtained from this grant have been forwarded to Air Force Research Laboratory (AFRL) NDE branch for possible transition to applied research.

PERSONNEL

Faculty: Prof. Victor Giurgiutiu (Feb. 15, 2004 to May 30, 2006); Prof. Yuh Chao (June 1, 2006 to June 30, 2007)

Post-Doc: Dr. Lingyu Yu (April 1, 2006 to June 30, 2007)

Graduate students: Bin Lin; Buli Xu; Cuc Adrian; Lingyu Yu (Feb. 15, 2004 to March 31, 2006); Santoni Bottai Giola; Weiping Liu

PRINCIPAL INVESTIGATOR (PI) TIME

The funded research has been conducted by Dr. Victor Giurgiutiu, Principal investigator (PI) in the Laboratory for Adaptive Materials and Smart Structures (LAMSS), and by Dr. Yuh Chao, Principal investigator (PI), at the University of South Carolina. Professor Giurgiutiu was PI for the period February 15, 2004 through May 30, 2006 when he was assigned to the Air Force Office of Scientific Research. Subsequently, Professor Chao became PI for the period June 1, 2006 through June 30, 2007.

The PIs have taken the main responsibility of the project, participated directly in its development, and mentored and advised the project participants. PI Professor Giurgiutiu and PI Professor Chao have devoted 3 months and 1.5 months of academic time to the project, respectively. Only the summer time has been budgeted to the AFOSR. The academic time is cost shared.